Title
Enhanced stem cell niche through microporous annealed particle scaffolds

Author
Koh, Jaekyung

Publication Date
2019

Peer reviewed|Thesis/dissertation

UNIVERSITY OF CALIFORNIA

Los Angeles

Enhanced stem cell niche through microporous annealed particle scaffolds

A dissertation submitted in partial satisfaction of the requirements for the degree Doctor of philosophy in Bioengineering

by

Jaekyung Koh

2019

ABSTRACT OF THE DISSERTATION

Enhanced stem cell niche

through microporous annealed particle scaffolds

by

Jaekyung Koh

Doctor of Philosophy in Bioengineering

University of California, Los Angeles, 2019

Professor Dino Di Carlo, Chair

Although stem cell therapy holds promises for intractable diseases, its efficacy has been limited by low retention and function of transplanted cells. Two of the key challenges for cell-based therapies are localization and cell function control once injected in a patient. Co-delivery of cells with hydrogels can mitigate these issues by localizing cells at a disease site and enhancing retention. However, the gold standard method, *in situ* gelation after injection with cells, confines transplanted cells and secreted therapeutic molecules within scaffolds due to the nanoporous nature of the hydrogel mesh.

Confined cells are confounded from participating in regeneration, leading to poor outcomes. Moreover, it has been challenging to modulate the biophysical properties of such hydrogels independently from porosity for effective stem cell functional control.

Here we show that microparticle scaffolds that can be co-injected locally with therapeutic cells and assembled *in situ* to generate a stem cell niche with interconnected microscale pore networks automatically formed in the void space between packed spherical particles. This approach enables enhanced migration and cell-cell connections between cells and transport of therapeutic molecules as well as higher cell proliferation *in vitro* and retention *in vivo*. Another key point is the modulation of biophysical properties independently from microporosity. Our scaffold provides a tunable porous environment by changing the physical properties of hydrogel building blocks. Using this platform technology, we demonstrated increased cell activity, such as proliferation and secretion, while the microporosity of the scaffolds induced tissue infiltration and vascularization. This approach achieves localized delivery of stem cells in a non-invasive manner creating a highly-tunable stem cell niche *in situ* which we envision can advance stem cell therapies as well as other cell-based therapies.

The dissertation of Jaekyung Koh is approved.

Steven M Dubinett

Zhen Gu

Stephanie Seidlits

Dino Di Carlo, Committee Chair

University of California Los Angeles

2019

DEDICATION

This work is dedicated to people around me, who supported me along the way. First of all, I would like to thank my mentor, Dr. Dino Di Carlo. He truly demonstrated my role model as a great researcher in the biomedical engineering field with entrepreneurship mind. The way he defines, approaches and solves problems deeply inspired and shaped me to pursue strong translational research. Also, I appreciate his patience and positive attitude along the process, that gave me a high motivation to keep moving forward.

Second, I am thankful to people who I interacted with and learned from during my Ph.D. research. Dr. Westbrook Weaver, Dr. Donald Griffin, and Dr. Philip Scumpia taught me essential and extensive knowledge and skill sets. Their professional communications and work performance motivated me to pursue them. Joe de Rutte and Maani Archang always surprised me with their great understanding, creative thoughts and critical discussions. Dr. Jun Fang and Dr. An-Chieh Feng demonstrated great and strong collaboration. I appreciate the help of Wei Yang, Thomas Horn, Michael Margolis, David Zalazar for their input, experiments, and discussions. I am also grateful to my committee members: Dr. Steven Dubinett, Dr. Stephanie Seidlits, Dr. Zhen Gu for their critical feedback on research progress and results, helpful suggestions. This broadened my view and helped to conduct highly interdisciplinary research.

Third, I would like to thank my friends, who shared my happiness, sadness and gave me a strong sense of belonging to society. I spent great times with my friends in the

Bioengineering department and Korean Graduate Student Association in house parties, Friday night hanging outs, ski trips, and K-town dinners. The sense of belonging and friendship was the main source that made my time and life here enjoyable and energetic.

Last, my highest dedication goes to my family: mom, dad, and brother. My parents raised, educated and guided me with their sensible caring and supports. My values that were deeply rooted from them made me explore and pursue my dream with curiosity and full of positive attitudes. I also thank my brother, who has been always supportive of my parents and me. Without them, I would not be able to be here.

TABLE OF CONTENTS

ACKNOWLEDGMENTS

Chapter 2-5 contains the manuscript submitted: Jaekyung Koh, Donald R. Griffin, Maani Archang, An-Chieh Feng, Thomas Horn, David Zalazar, Michael Margolis, Hamed Haddadi, Tatiana Segura, Philip O. Scumpia, Dino Di Carlo, “Enhanced function of a stem cell niche through self-assembly of injected monodisperse hydrogel particles into a modular microporous scaffold.” J.K., D.R.G., T.S., D.D.C. conceived the study and designed the experiment. J.K., M.A. performed in vitro studies, J.K., D.R.G., A.F., P.O.S. performed *in vivo* studies. J.K., T.H., M.M., D.Z., H.H. characterized the MAP scaffold. J.K. designed and fabricated the microfluidic device. J.K., D.D.C. analyzed and interpreted the data. J.K. and D.D.C. wrote the manuscript with input from all the authors. This work was supported by the Presidential Early Career Award for Scientists and Engineers (N00014-16-1-2997). J.K. was supported by the Kwanjeong Educational Foundation, Korea. P.O.S. was supported by the Mentored Clinical Scientist Development Award (K08-AR066545) through NIAMS. The authors would like to thank Weikun Xiao and Dr. Stephanie Seidlits for technical assistance and comments, Dr. Jason Lee at the Crump Institute in California NanoSystems Institute (CNSI) for discussions and assistant for IVIS, Dr. Matt Schibler and Dr. Laurent Bentolila at Advanced Light Microscopy/Spectroscopy in CNSI for confocal imaging consultation, Dr. Westbrook Weaver, Joseph de Rutte, Dr. Maria Antfolk and Wei Yang for helpful discussions.

VITA

EDUCATION

University of California, Los Angeles (UCLA)

- M.S. in Bioengineering (2017)

Seoul National University (SNU)

- M.S. in Electrical Engineering (2014)
- B.S. in Electrical Engineering (2012)
- B.S. in Technology Management (2012)

RESEARCH EXPERIENCE

Graduate Student Researcher (2014-2019), UCLA Bioengineering

Advisor: Dino Di Carlo, Ph.D.

Graduate Student Researcher (2012-2014), SNU Electrical Engineering

Advisor: Sunghoon Kwon, Ph.D.

PUBLICATIONS

[5] **Jaekyung Koh**, Donald R. Griffin, Maani Archang, An-Chieh Feng, Thomas Horn, David Zalazar, Michael Margolis, Hamed Haddadi, Tatiana Segura, Philip O. Scumpia, Dino Di Carlo, “Enhanced function of a stem cell niche through self-assembly of injected monodisperse hydrogel particles into a modular microporous scaffold,” (submitted)

[4] Joseph de Rutte, **Jaekyung Koh**, Dino Di Carlo, “Scalable high-throughput production of modular microgels for in situ assembly of microporous tissue scaffolds,” (in revision)

[3] Jin-Wook Lee, Zhenghong Dai, Changsoo Lee, Hyuck Mo Lee, Tae-Hee Han, Nicholas De Marco, Oliver Lin, Christopher S. Choi, Bruce S. Dunn, **Jaekyung Koh**, Dino Di Carlo, Jeong Hoon Ko, Heather D. Maynard, and Yang Yang, “Tuning Molecular Interactions for Highly Reproducible and Efficient Formamidinium Perovskite Solar Cells via Adduct Approach,” J. Am. Chem. Soc. 140, 6317–6324 (2018).

[2] **Jaekyung Koh**, Chueh-Yu Wu, Harsha Kittur, Dino Di Carlo, “Research highlights: microfluidically-fabricated materials,” Lab Chip 15, 3818-3821 (2015).

[1] Janay Elise Kong, **Jaekyung Koh**, Jonathan Lin, Dino Di Carlo, “Research highlights: translating chips,” Lab Chip 15, 1984-1988 (2015).

CONFERENCE PROCEEDINGS (SELECTED)

[5] **Jaekyung Koh**, Donald Griffin, An-Chieh Feng, Thomas Horn, Michael Margolis, Hamed Haddadi, Maani Archang, Tatiana Segura, Philip Scumpia, Dino Di Carlo, “Enhanced function of a stem cell niche through self-assembly of injected monodisperse hydrogel particles into a highly-modular microporous scaffold,” Bioengineering Research Day, University of California, Los Angeles, CA, Feb. 2019. **[Podium Presentation]**

[4] **Jaekyung Koh**, Donald Griffin, An-Chieh Feng, Thomas Horn, Michael Margolis, Hamed Haddadi, Maani Archang, Tatiana Segura, Philip Scumpia, Dino Di Carlo, “Maintenance of Implanted Mesenchymal Stem Cell Function using Injectable Monodisperse Hydrogel Particles Assembled into a Microporous Scaffold,” 2018 IEEE EMBS Micro and Nanotechnology in Medicine Conference, Koloa, Hawaii, Dec. 2018.

[3] **Jaekyung Koh**, Donald Griffin, An-Chieh Feng, Thomas Horn, Michael Margolis, Hamed Haddadi, Tatiana Segura, Philip Scumpia, Dino Di Carlo, “Long-term maintenance of an allogeneic mesenchymal stem cell niche through self-assembly of injected monodisperse hydrogel particles into a microporous scaffold,” 2018 MRS Fall Meeting, Boston, MA, Nov.2018. **[Podium Presentation]**

[2] **Jaekyung Koh**, Donald Griffin, An-Chieh Feng, Philip Scumpia, Tatiana Segura, Dino Di Carlo, “Injectable microporous scaffold for long-term stem cell niche,” SoCal Micro and Nanofluidics Symposium, Irvine, CA, Aug.2017. **[Podium Presentation]**

[1] **Jaekyung Koh**, Westbrook Weaver, Dino Di Carlo, “Microfluidically-fabricated flowable microporous hydrogel scaffolds for 3D tissue culture,” 2016 Society for Laboratory Automation and Screening (SLAS) Conference, San Diego, CA, Jan.2016. **[Podium Presentation]**

SELECTED AWARDS & HONORS

Kwanjeong Fellowship, Kwanjeong Educational Foundation, Seoul, Korea (2014-2019)

UCLA Bioengineering Fellowship, UCLA Bioengineering (2014)

Distinguished Dissertation Award, School of Electrical Engineering, SNU (2014)

Graduation with honors, *Cum Laude*, SNU (2012)

Chapter 1. Microenvironments for Cell Therapies

1.1 Stem-cell therapies

Stem cells are unspecialized cells with the capability to replicate themselves for long periods without significant changes in their general properties and can differentiate into various specialized cell types under certain physiological or experimental conditions. Since the discovery of stem cells, owing to their ability to generate tissue de novo following disease or injury, there has been growing interest of developing stem cell–based therapies for various degenerative diseases.

Among stem cells, mesenchymal stem cells (MSCs) are an excellent candidate for cell therapy for following reasons[1]. First, human MSCs are easily accessible and the isolation of MSCs is straightforward. Moreover, the cell expansion to clinical scales can be done in a relatively short period of time as well as being preserved with minimal loss of potency and stored for point-of-care deliver. Last, human trials of MSCs thus far have shown no adverse reactions to allogeneic versus autologous MSC transplants, enabling creation of an inventory of third-party donor MSCs to widen the number of patients treated by a single isolation.

With the properties stated above, stem cell therapies hold promise for numerous intractable diseases in regenerative medicine through a number of routes, such as promotion of tissue repair and modulation of the immune system[1–4], and its clinical translation has been widely explored[25]. The therapeutic properties of MSCs include anti-apoptosis, angiogenesis, growth factor production, neuroprotection, anti-fibrosis, and

chemo-attraction, which provides a broad spectrum for their potential in disease therapies. MSC clinical trials can be mainly divided into the following cases:

i) Immune suppressive properties: MSCs' functions of suppressing activated T cell proliferation and their cytokine production, increasing regulatory T cells (Tregs) that dampen killer T cell attack on foreign cells or tissues can be utilized for containment of immune rejection in allogeneic grafting
ii) Myocardial injury benefits: MSCs demonstrate a therapeutic effect for cardiovascular repair, particularly a benefit to patients with severe myocardial infarct
iii) Osteoarthritis and lower back pain: bone marrow MSCs would be expected to contribute to bone and cartilage repair
iv) Pulmonary disease: the levels of inflammatory cytokines were significantly reduced in lung aspirates after transplantation
v) Liver disease and diabetes
vi) Ischemic stroke and ALS

MSCs participate in the regeneration mainly by two mechanisms: direct differentiation into a desired cell type and therapeutic molecule secretion (Fig. 1-1). The multilineage potential of MSCs is the cornerstone for their use in tissue regeneration[6]. Upon injection, undifferentiated MSCs migrate to the site of injury and differentiate to cells of the appropriate phenotype under the influence of local signals[7]. However, their inherent ability to differentiate into a variety of cell phenotypes is not the only characteristic that makes these cells attractive for therapeutic purposes. The secretion of a broad of bioactive molecules by MSCs, such as growth factors, cytokines and chemokines, that

modulate the molecular composition of the environment to evoke responses from resident cells, constitutes their most biologically significant role under injury conditions[8–10]. Specifically, these secreted molecules suppress the local immune system, inhibit fibrosis or scar formation, apoptosis, enhance angiogenesis, and stimulate mitosis and differentiation of tissue-intrinsic reparative or stem cells[11].

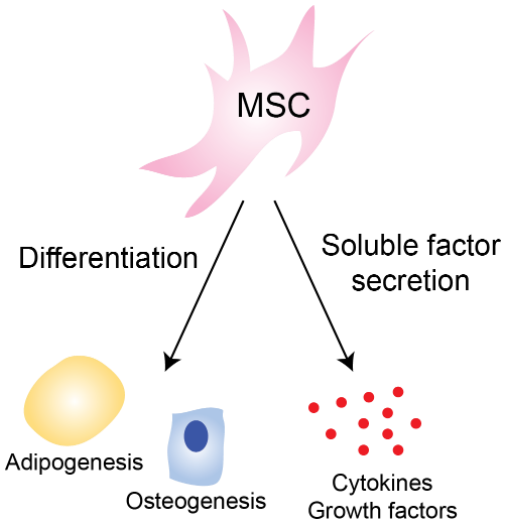

Figure 1-1 Two main regeneration mechanisms by MSCs. The multilineage potential to differentiate to cells of the appropriate phenotype and the ability to secrete therapeutic molecules to evoke responses from resident cells are widely adapted in MSC therapies.

1.2 Stem cell niche

Despite substantial advances in our understanding of MSCs and extensive trials of MSCs for therapeutic applications, several challenges remain that limit the widespread clinical use of stem cells or specifically MSCs. Its clinical translation has been

challenging due to poor survival and engraftment of transplanted stem cells to a disease site[12–15]. Moreover, loss of control by the engrafted cells in a disrupted biological environment limits the ability to harness the stem cells for meaningful therapeutic outcomes[5,16]. Current hurdles to the clinical translation of stem cell therapies include not only maintenance of the stem cell state, reproducible expansion of large numbers of stem cells for transplantation, but also efficient control of the cell state both pre- and post-transplantation, and protection of the cells during and after delivery to patients. To maximize the efficacy of MSC therapies, we would need to understand how endogenous stem cells interact and behave in their surrounding cell microenvironment. In other words, the ability to manipulate interactions between stem cells and their local environment in order to regulate and direct stem cell function will be a key aspect for stem cell-based therapies.

Understanding the native environment of adult stem cells provides clues how to manipulate stem cells and enhance the efficacy of stem cell-based therapies. In the native environment, cells are surrounded by an extracellular matrix (ECM), which provides biochemical signals and a structure for physical cell-matrix interactions to occur (Fig. 1-2). In fact, cells actively degrade, deform and remodel their ECM sense its mechanical strength and porosity, and go through lineage-specific differentiation along with various biophysical signals. In detail, the sensory machinery of stem cells can sense and process multiple signals simultaneously from their niche and convert them to a coherent environmental signal to regulate downstream gene expression and stem cell fate[17]. Although the underlying signaling pathways are still a matter of debate, cell-

generated traction forces is believed to play an integral role in detecting biophysical cues and in inducing subsequent differentiation[18].

Creating specialized microenvironments or stem cell niche *in situ* for stem cell manipulation is a promising strategy. It can increase the cell survival after transplantation and induce cell migration, deployment and activities by providing proper biophysical and biochemical signals from the niche. An artificial niche that provides proper soluble and surface bounding signal factors as well as mechanical signals and induces cell-cell contacts such that it maximizes the therapeutic effects of transplanted stem cells would be a key question for enhanced stem cell therapies.

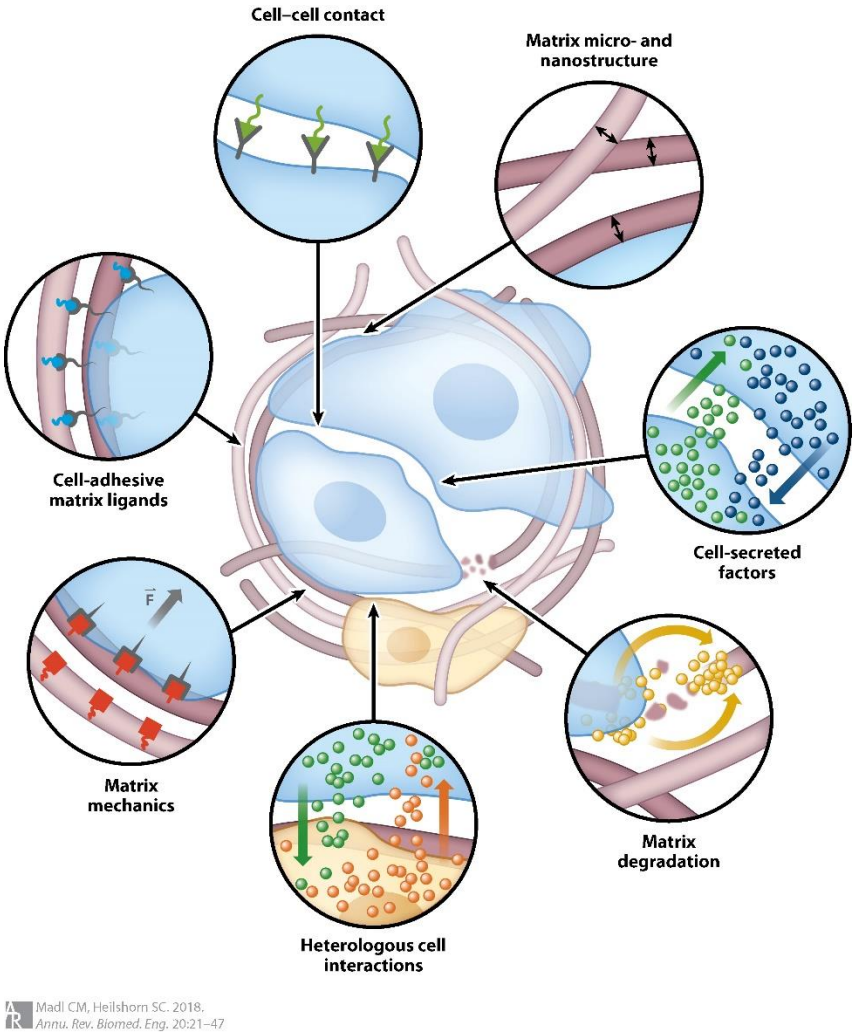

Figure 1-2 Niche interactions known to modulate stem cell phenotype[19]. Stem cells, their differentiated progeny, and other supporting cell types within the niche interact via secretion of soluble factors and direct cell-cell contact, modulating the biochemical signaling pathways that regulate maintenance of the stem cell pool and control differentiation into mature phenotypes. Reproduced with permission from the Annual Review of Biomedical Engineering.

However, in clinical settings, often stem cells are injected systemically, thus not being able to provide proper biophysical and biochemical components for engraftment and differentiation of MSCs. Recent studies suggested that less than 1% of systemically

administered MSCs persist for longer than a week following injection, and more than 80% of injected MSCs were trapped in lungs[1] (Fig. 1-3). These experiments demonstrate the necessity to develop a bioengineered approach to achieve localized delivery of stem cells as well as modulating cell functions *in situ*.

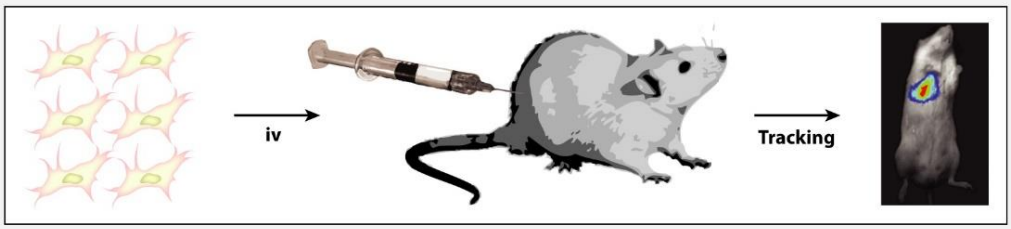

Time after iv injection	Lungs	Heart	Spleen	Liver	Nodes	Kidneys	Gut
	Lee et al. 2009 (Ref. 14)						
1 h	83%	<1%	<1%	<1%	<1%	<1%	<1%
24 h	42%	~0%	~0%	~0%	~0%	~0%	~0%
7 days	<0.01%	~0%	~0%	~0%	~0%	~0%	~0%
30 days	~0%	~0%	~0%	~0%	~0%	~0%	~0%
	Zangi et al. 2009 (Ref. 15)						
5 days	1%	~0%	<1%	~0%	~0%	~0%	~0%
10 days	1%	~0%	~0%	0.5%	~0%	~0%	~0%
20 days	<0.25%	~0%	~0%	<0.5%	~0%	~0%	~0%
30 days	~0%	~0%	~0%	<0.1%	~0%	~0%	~0%

Parekkadan B, Milwid JM. 2010.
Annu. Rev. Biomed. Eng. 12:87–117

Figure 1-3 Representative studies describing the *in vivo* distribution of MSCs upon systemic administration. Tracking studies generally consist of intravenous injection of the cells and then tracking of the cells using a variety of known methods. The representative studies featured here used two sensitive methods available for whole-

organism analysis: polymerase chain reaction of a human gene to quantify human MSC engraftment in a number of mouse tissues, and MSCs labeled with luciferase to qualitatively trace their engraftment. Reproduced with permission from the Annual Review of Biomedical Engineering.

1.3 Artificial stem cell niche using biomaterials

Delivery of stem cells with biomaterials can be a promising strategy (Fig. 1-4). Upon injection, biomaterials can provide a suitable cell microenvironment to mitigate the main hurdles limiting the clinical translation of cell transplantation such that biomaterials increase cell survival and migration as well as inducing integration of cells[20]. Moreover, biomaterials can influence local angiogenesis and modulate the immune response with the strategies aimed at influencing the host tissue niche. Advances in materials science have enabled unprecedented control over the biochemical and biophysical properties of materials used for stem cell therapies. Material properties can be tuned to create an artificial niche to both expand naive stem cells and efficiently differentiate stem cells into mature cell types. Among biomaterials, hydrogels are widely adopted due to high water content (typically 70-99%), physical similarity to tissues, and excellent biocompatibility[21].

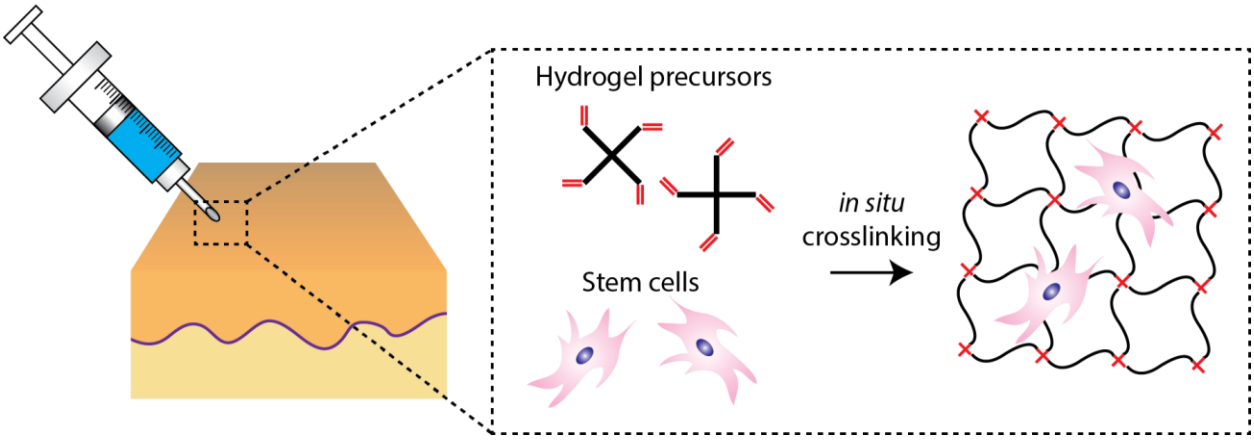

Figure 1-4 Localized delivery of stem cells with hydrogel precursors. In-situ crosslinked hydrogels may provide proper ECM components to enhance stem cell survival and function.

An ideal material should not only enable minimally invasive delivery by injection, and retain cells after transplantation to achieve sustained secretion, but also create an artificial stem cell niche *in situ* for higher efficacy and longer maintenance of the therapy[20,22]. Specifically, the biomaterial should provide suitable biophysical and biochemical microenvironmental cues for enhanced control of cell function *in vivo*[23,24].

However, current injectable biomaterials suffer from ineffective modulation[25] or lack of porosity for mass transport, cell motility, proliferation, cell-cell adhesion, or new tissue formation[26–29]. The gold standard method, *in situ* gelation after injection with cells, confines transplanted cells and secreted therapeutic molecules within scaffolds due to the nanoporous nature of the hydrogel mesh. To mitigate the nanoporous gel mesh and promote cell motility, infiltration and vascularization, lightly crosslinked matrix can be approached; however, this often results in unstable mechanical stability and integration, thus possessing limited function as a stem cell niche. In addition, the modulation of

physical properties, such as stiffness, often changes the porosity of hydrogels, thus limiting the effective control over cell behaviors using biophysical cues.

Chapter 2. Stem cell niche formation using microporous annealed particle scaffolds

2.1 Introduction

The fundamental challenges that the independent modulation of physical properties from hydrogel porosity was introduced in the previous chapter. To mitigate the issues, the microporous annealed particle (MAP) scaffold, a new class of biomaterial from self-assembly of hydrogel microparticles developed by Griffin et al.[30] is reviewed. For an effective stem cell niche generation *in situ*, how MAP scaffolds can be utilized is discussed.

2.2 Microporous annealed particle (MAP) scaffolds

Delivered as a liquid and polymerized *in situ*, previous injectable scaffolds possessed a fundamental trade-off between overall mechanical strength and porosity/degradability enabling tissue ingrowth[31]. Highly-crosslinked scaffolds that can maintain a structural support often result in reduced cell migration and ingrowth. Generating micropores in a scaffold promotes cellular infiltration while separately modulating bulk material properties[32]; nonetheless these microporous scaffolds generated using leaching methods must be manufactured *ex situ*[33].

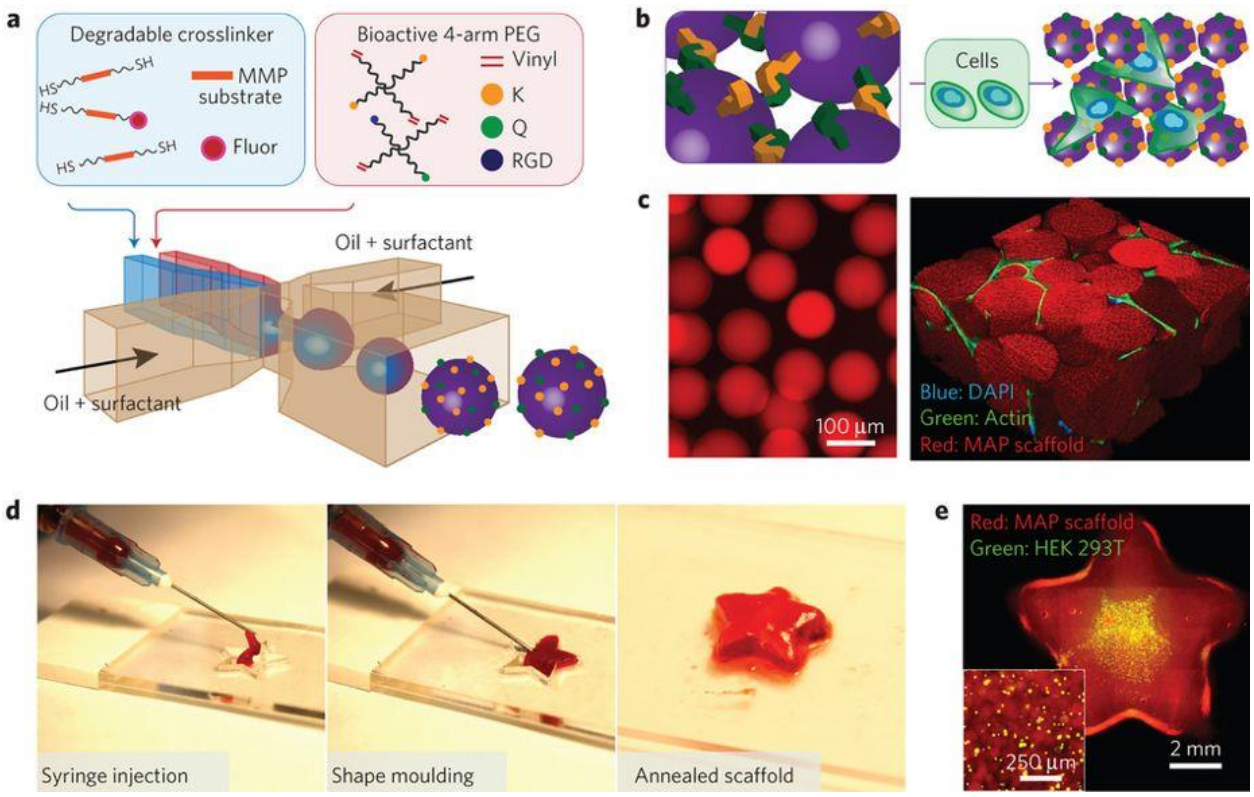

Figure 2-1 Microfluidic generation of microsphere hydrogel building blocks for the creation of microporous annealed particle (MAP) scaffolds. (a) Scheme illustrating microgel formation using a microfluidic water-in-oil emulsion system. A pre-gel and crosslinker solution are segmented into monodisperse droplets followed by in-droplet mixing and crosslinking via Michael addition. (b) Microgels are purified into an aqueous solution and annealed using FXIIIa into a microporous scaffold, either in the presence of cells or as a pure scaffold. (c) Fluorescent images showing purified microgel building blocks (left) and a subsequent cell-laden MAP scaffold (right). (d) MAP scaffolds are mouldable to macroscale shapes, and can be injected to form complex shapes that are maintained after annealing. (e) This process can be performed in the presence of live cells. Reprinted with permission from Macmillan Publishers Ltd: Nature Materials. Griffin et al., Nat. Mater., 2015, 14, copyright 2015.

Griffin et al. tackled these issues with a bottom-up approach: creating a scaffold from microfluidically-fabricated building blocks[34]. Produced by a microfluidic water-in-oil emulsion method (Fig. 2-1), uniform microsphere scaffold building blocks are polymerized, collected and brought into an aqueous solution where they are subsequently injected and annealed to one another enzymatically forming a Microporous Annealed Particle (MAP) gel (Fig 2-1b and c). Micropores form as the network of void spaces between the covalently linked spherical gel particles. These building blocks are composed of a synthetic hydrogel mesh of multi-armed poly(ethylene) glycol-vinyl sulfone (PEG-VS) backbone decorated with cell-adhesive peptide (RGD), protease substrate crosslinkers, and two transglutaminase peptide substrates (K and Q). *Via* crosslinking of K and Q peptides by thrombin-activated Factor XIII, an enzyme responsible for blood clotting, these neighboring blocks dynamically form the MAP scaffold *in situ* with a seamless interface (Fig. 2-1d and e).

The chemical and physical properties of the scaffold can be tailored through microfluidic fabrication. The microporosity of the scaffold was modulated by the size of building blocks, which the authors precisely controlled with flow rate and geometry of the microfluidic device. The manipulation of storage moduli was achieved by varying PEG weight percentages and crosslinker stoichiometries, which were introduced into two separate inlet channels within the microfluidic device and only mixed once a droplet was formed. As a result, the moduli spans the stiffness regime necessary for mammalian soft tissue mimetics. In addition, the degradation of the scaffold was determined by the combination of microporosity and physical properties of the MAP gels.

The authors first demonstrated that cells could be seeded directly within the MAP gels prior to annealing, and following annealing extensive three-dimensional cellular networks rapidly formed for three human cell lines. They observed that cell networks increased in size and complexity through the entirety of the experiment and growth rate and cellular network formation greatly exceeded identical conditions with a non-porous gel. Furthermore, they were able to deliver the microgel building blocks directly to a wound site in murine skin by syringe injection, and found that the annealed MAP scaffold accelerated wound closure compared to control conditions or non-annealed scaffold by host-cell recruitment through microscale porosity. These results clearly support that the MAP scaffold prompts *in vitro* and *in vivo* cell spreading and migration as well as bulk tissue integration.

An important point is that imperfect self-assembly of the microgel building blocks leads to a robust formation of a porous scaffold, solving many issues with other bottom-up biomaterial approaches. Beyond wound healing, microfluidic-control over the building block generation provides a new bottom-up framework in tissue engineering scaffold fabrication; the self-assembled scaffold *in situ* combines the benefits of injectability, microporosity and modularity. Overall, this novel scaffold gel should be able to improve tissue regeneration, organ-on-a-chip technologies, as well as stimulating clinical research and applications in wound healing.

2.3 Hypotheses for the use of MAP scaffolds as a stem cell niche

We present the development of a tunable and injectable microporous stem cell niche using microporous annealed particle (MAP) scaffolds. MAP scaffolds were shown to accelerate regeneration by providing microscale interconnected pore spaces for cell migration from the surrounding tissue as well as reducing the inflammatory response[35–38].

When subcutaneously implanted without cells, we obtained additional evidence that MAP scaffolds induced tight integration with surrounding tissue, observed by collagen deposition and vascularization deep into the scaffold volume compared to the fibrous encapsulation observed for a chemically-identical non-porous scaffold (Fig. 2-2).

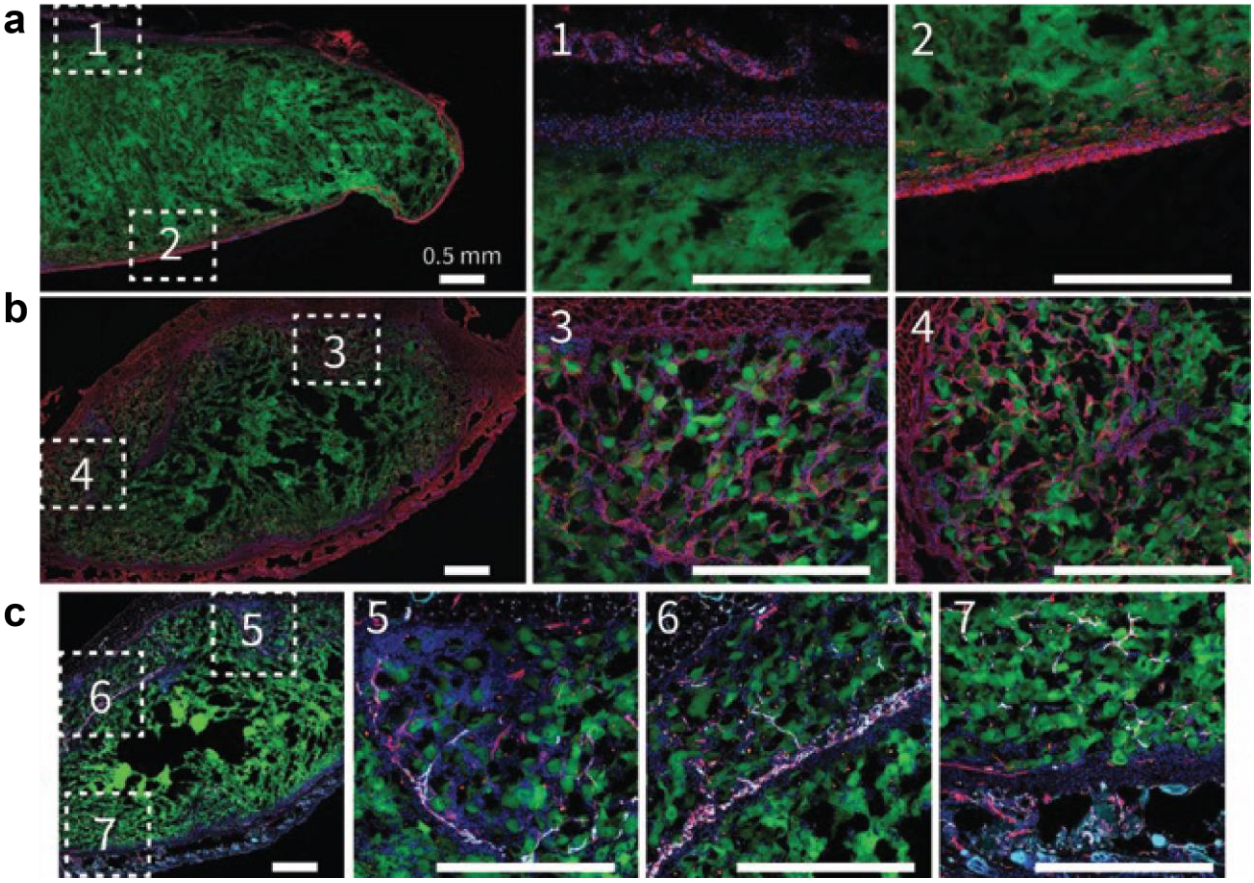

Figure 2-2 Tissue infiltration and vascularization into non-porous scaffolds and microporous annealed particle (MAP) scaffolds without co-delivered cells. **a** Collagen deposition is concentrated around the edge of non-porous scaffolds following two weeks of implantation. **b** Collagen deposition extends deeper into MAP scaffolds following two weeks of implantation. In a, b, Type III Collagen staining (red), nucleus (blue), hydrogel (green). **c** Visualization of vascularization into the MAP scaffold following two weeks of implantation shown by CD31/PECAM staining (magenta). Nucleus (blue), hydrogel (green). Image 1 ~ 7 are inset images from the first image of each row. Scale bars: 500 μm.

Non-porous (material control) and MAP scaffolds (M) were injected subcutaneously without the addition of cells or growth factors. After two weeks, non-porous scaffolds

demonstrated a fibrous capsule surrounding the hydrogel with very little in-growth of cells or tissue (a). MAP gel scaffolds demonstrated a minimal fibrous capsule, and demonstrated tremendous ingrowth of Collagen 3 expressing cells, as well as collagen deposition (b). This was accompanied by blood vessel formation within the hydrogel scaffold as demonstrated by PECAM staining (c). These findings suggested that MAP hydrogels may represent a novel delivery system for stem cell-based therapies to tissue *in vivo*.

With these results considered, we were motivated to apply MAP scaffolds as a cell delivery vehicle for enhanced function of stem cells (Fig. 2-3a). Delivered with mesenchymal stem cells (MSCs), monodisperse hydrogel microparticles were enzymatically assembled *in situ*, generating a highly-controlled interconnected microscale pore space, where cells quickly migrate, adhere, and proliferate, leading to enhanced survival of transplanted cells *in vivo*. Moreover, we show that the material properties can be tuned to promote the maintenance of the stem cell population while integrating with surrounding tissues through vascularization. We anticipate that this approach can be easily translated and generally applied to delivery of other therapeutic cells, given cell production can be independent of biomaterial production, and molecularly and biophysically tailored niches can be created.

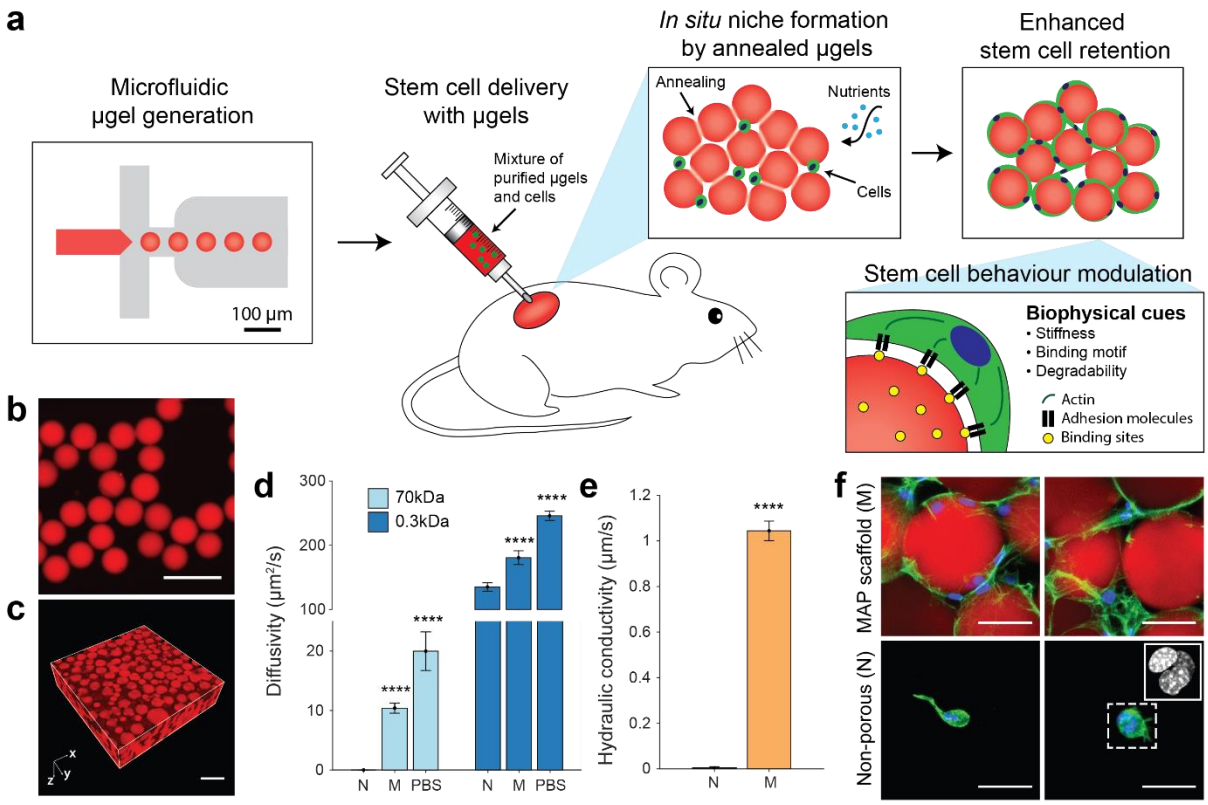

Figure 2-3 Mesenchymal stem cell (MSC) delivery and in situ niche creation strategy using annealed monodisperse hydrogel particles. **a** An artificial stem cell niche is created *in situ* from annealing of a suspension of injectable monodisperse hydrogel particles. Highly monodisperse particle building blocks enable the generation of a pore network in a highly controllable manner, which promotes the transport of oxygen and nutrients as well as cell migration. The biophysical properties of building blocks are modulated to enhance the functions of the transplanted MSCs. **b** Monodisperse hydrogel particles or μgels produced by the microfluidic device. Scale bar: 200 μm. **c** Tissue scaffold assembled from monodisperse μgels. Scale bar: 200 μm. **d** Diffusivity of 70 kDa dextran and 0.3 kDa FITC in non-porous scaffold (N), MAP scaffold (M) and PBS (n = 4 - 7). Data are presented as average ± s.d. Statistical significance based on one-way ANOVA followed by Tukey's HSD *post hoc* test (significance compared to N, ****p < 0.0001). **e** Hydraulic conductivity of PBS through the non-porous scaffold (N) and MAP scaffold (M) at the atmospheric pressure (n = 3). Data are presented as average ± s.d. Statistical significance based on standard two-tailed Student t-test (****p

< 0.0001). **f** Fluorescent images of MSCs *in vitro* cultured in microporous scaffolds and non-porous scaffolds at week 2. Blue, nucleus; Green, actin; Red, gel. Scale bar: 50 μm.

Chapter 3. MAP scaffold characteristics

3.1 Introduction

The nature of interconnected pore space in MAP scaffolds can induce cells migration, adherence and proliferation for enhanced stem cell function. In this chapter, the pore network is investigated as well as mass transport by diffusion and convection is measured to demonstrate the characteristics of MAP scaffolds that are favorable for cell expansion and retention.

3.2 Interconnected micropore network

We hypothesized that covalently-linked assemblies of monodisperse hydrogel particles would produce an interconnected pore space with more regular and controlled structure. Highly-monodisperse (CV < 5%) microscale hydrogel particles were generated using a microfluidic approach (Fig. 2-3b and Fig. 3-1a, b). These particles were enzymatically annealed *in vitro* to generate monodisperse MAP (mono-MAP) scaffolds (M) (Fig. 2-3c, d). As a comparison, polydisperse particle suspensions with three different average diameters (CV > 35%) were generated by agitation (Fig. 3-1b, c) and annealed to form polydisperse MAP (poly-MAP) scaffolds (P1, P2 and P3) (Fig. 3-1). Mono-MAP scaffolds demonstrated a higher void fraction (Fig. 3-2) and a larger fraction of pore sizes larger than the cell diameter than poly-MAP scaffolds (Fig. 3-3). Since pore size below approximately one cell diameter can result in reduction in cell migration and

ability to spread within the scaffold[39], mono-MAP scaffolds were expected to induce higher cell migration and proliferation than poly-MAP scaffolds.

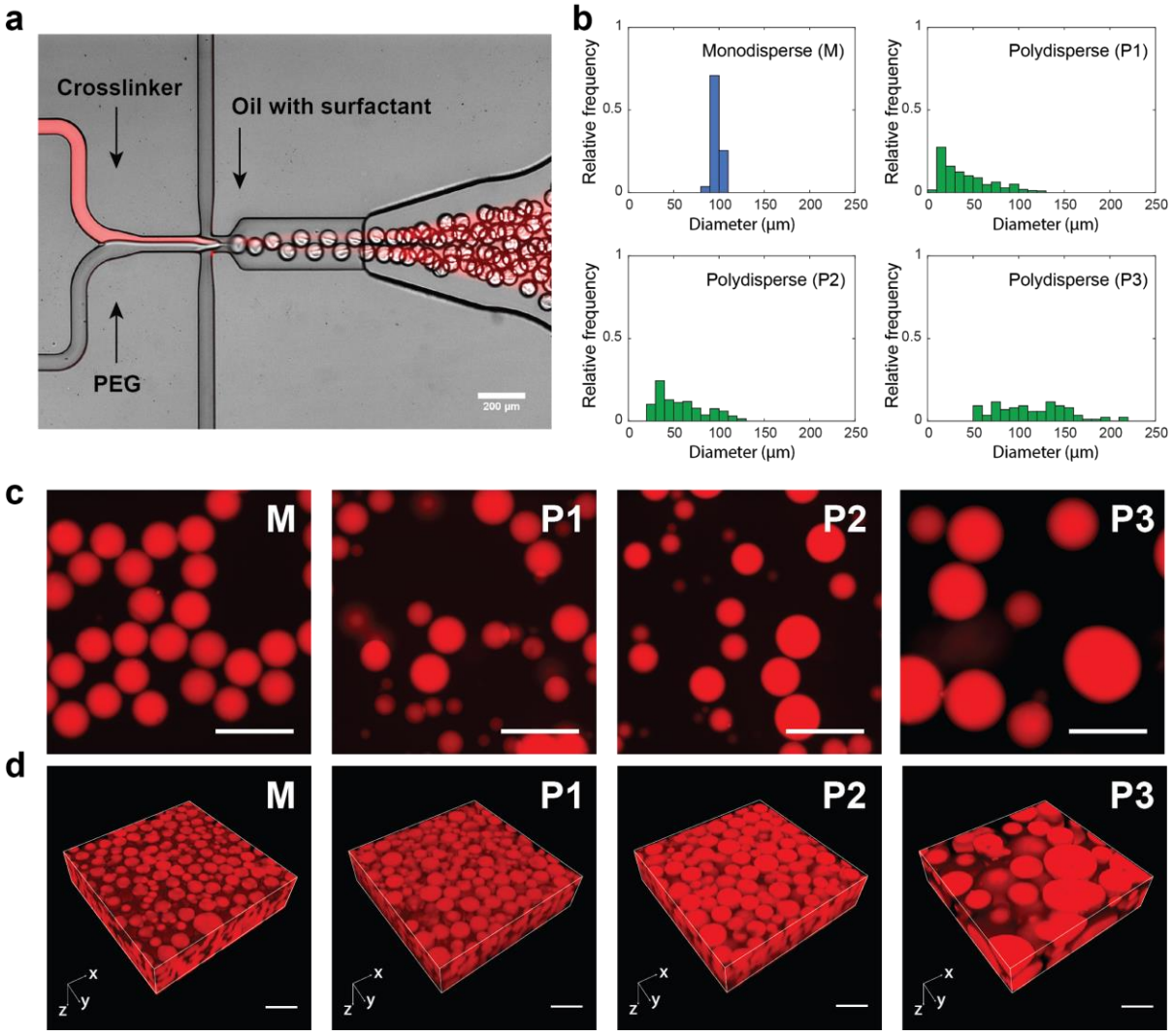

Figure 3-1 Hydrogel building blocks turned into tissue scaffolds. **a** Combined bright field and fluorescent (TRITC) images of monodisperse µgel generation in a microfluidic droplet generator. **b** The Size distribution of monodisperse and polydisperse µgels after swelling in HEPES buffer. **c** Fluorescent images of hydrogel particles of each type. **d** Fluorescent images of scaffolds assembled from building blocks of each type. Scale bar: 200 µm.

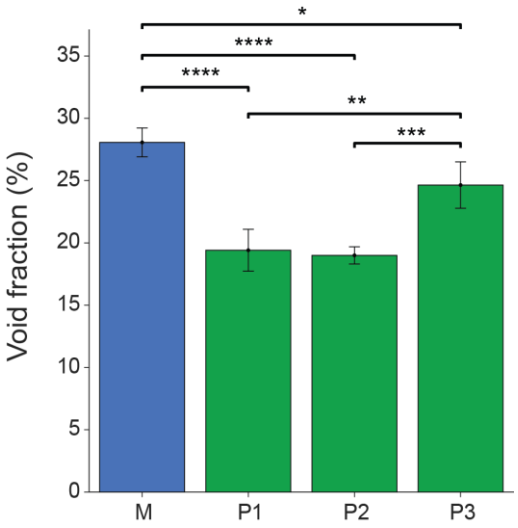

Figure 3-2 Void volume fraction in the MAP scaffold (M) and polydisperse MAP scaffolds (P1, P2 and P3) (n=4). Data are presented as average ± s.d. Statistical significance performed using one-way ANOVA followed by Tukey's HSD *post hoc* test (∗p<0.05, ∗∗p<0.01, ∗∗∗p<0.001, ∗∗∗∗p<0.0001).

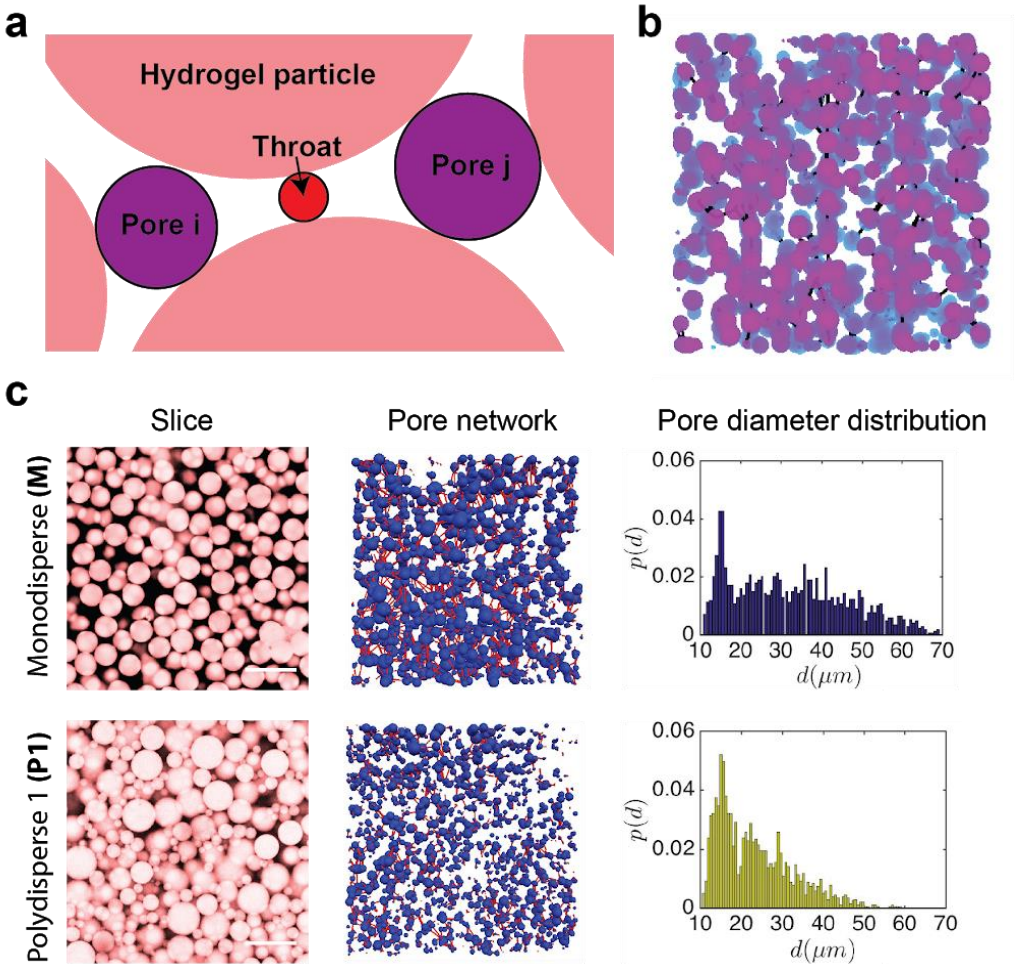

Figure 3-3 MAP Scaffold pore analysis. **a** Pore size analysis scheme using maximal ball algorithm. Pore i and pore j indicate the voids possessing a diameter that is the largest regionally found by an inflating search and are connected by smaller size inflated spheres that define a pore throat. **b** Visualization of pores (voids) and their connections. Purple balls indicate maximal balls corresponding the largest spherical void in the region and black lines indicate the connectivity between these voids. **c** Pore network and diameter distribution of a MAP scaffold (M) and a polydisperse MAP scaffold (P1).

3.3 Enhanced mass transport by diffusion

Interconnected microporosity present in MAP scaffolds we fabricate enables the transport of nutrients and oxygen and may overcome diffusion limitations of conventional non-porous hydrogels. To assess transport by diffusion, we performed fluorescence recovery after photobleaching (FRAP) using fluorescein (0.3 kDa) and dextran-conjugated fluorescein (70 kDa) (Fig. 2-3d and Fig. 3-4). The fluorescent intensity recovery was on the order of tens of seconds in MAP scaffolds, resulting in a calculated diffusivity for 70 kDa dextran approximately 50% of that in PBS, while no diffusion was detected into the hydrogel particles in the same timeframe. Given the relatively large hydrodynamic diameter of 70 kDa dextran that is comparable to the nanoscale pores in the gel mesh network, steric hindrance severely limits diffusion[21,40]. In fact, the observation of diffusion in macroscale gels revealed that the diffusivity was 50-fold lower than that in PBS (0.42 $\mu m^2/s$), in agreement with previous reports[41]. For 0.3kDa fluorescein molecules, MAP scaffolds again demonstrated a significantly enhanced diffusivity compared to chemically-matched non-porous gels (Fig. 2-3d).

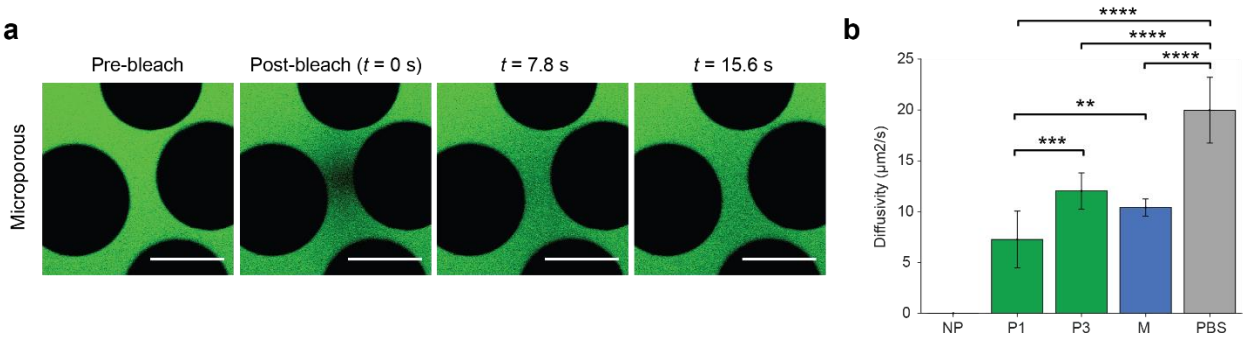

Figure 3-4 Diffusion measurement in the MAP scaffold using fluorescent recovery after photobleaching (FRAP). **a** Recovery of 70 kDa dextran-conjugated with FITC in the MAP scaffold. A spot comparable to the pore diameter was bleached and its recovery was measured over time. Black circles correspond to the area that was occupied by μgels. Scale bar: 50 μm. **b** Calculated diffusivity of 70 kDa dextran molecules from FRAP experiment. No diffusion was detected in a non-porous gel during the measurement time frame.

3.4 Enhanced mass transport by convection

Higher convective flux of fluid also resulted from the interconnected pore network of the scaffolds. To measure hydraulic conductivity, non-porous scaffolds and MAP scaffolds were placed on top of a membrane with 5μm pores in a custom-designed device which allowed for precise gravity-driven flow (Fig. 3-5). While only limited permeation was observed through the non-porous scaffold resulting in a conductivity of ~1.6 x 10^{-3} μm/s at atmospheric pressure, the interconnected porosity of MAP scaffolds yielded ~600-fold enhancement of the conductivity (~1 μm/s) (Fig. 2-3e), which was comparable to physiologic convection in the extracellular fluid[42]. This not only indicates that the pores

are interconnected throughout the scaffold, but also suggests that nutrients and waste can be transported by convection[43], which may be beneficial for cell survival and proliferation in a macroscale biomaterial formed from MAP gel *in vitro* and *in vivo*.

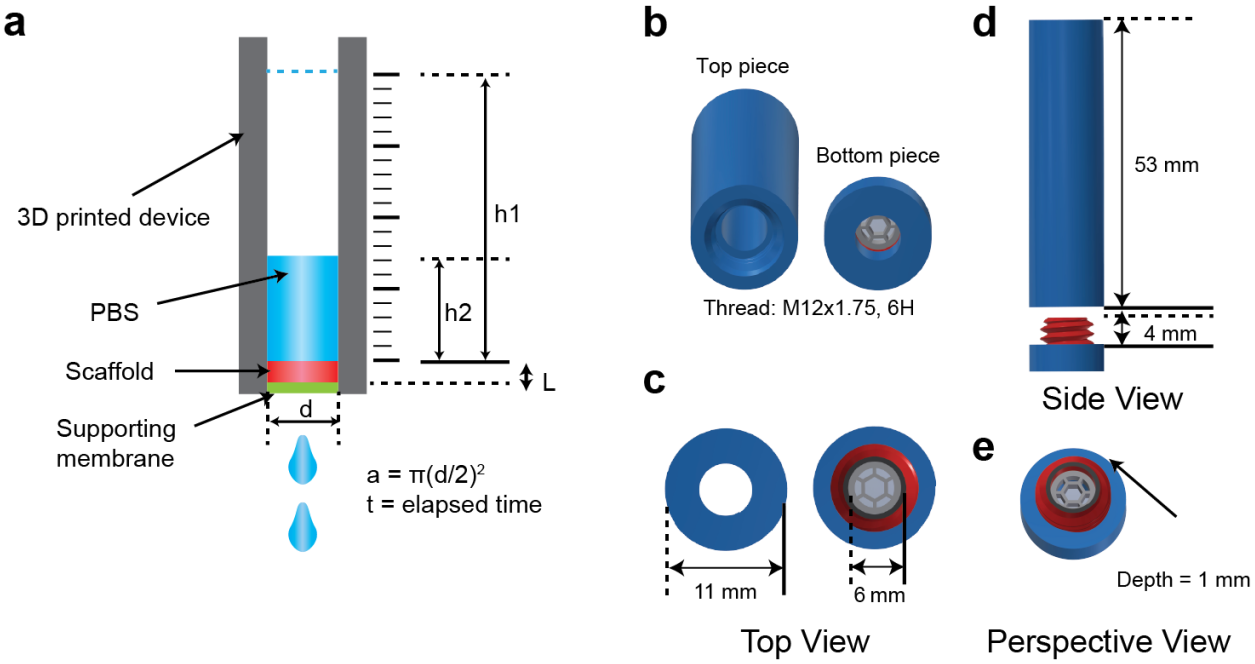

Figure 3-5 Hydraulic conductivity measurement. **a** Schematic of the hydraulic conductivity measurement using a 3D-printed device. Initial height (h1) and final height (h2) of PBS over elapsed time were recorded to calculate the conductivity. See Video S1 and S2. **b** Two components of a 3D-printed device viewed from **c** top, **d** side and **e** perspective.

3.5 Methods

Microfluidic device fabrication.

Microfluidic devices were fabricated using soft lithography as previously described[35]. Briefly, master molds were fabricated on mechanical grade silicon wafers (University wafer) using KMPR 1050 photoresist (Microchem). Devices were molded from the masters using poly(dimethyl)siloxane (PDMS) Sylgard 184 kit (Dow Corning). The base and crosslinker were mixed at a 10:1 mass ratio, poured over the mold, and degassed prior to curing for overnight at 65 °C. Channels were sealed by treating the PDMS mold and a glass microscope slide (VWR) with oxygen plasma at 500 mTorr and 80W for 30 seconds. The channels were functionalized by injecting 100µL of Aquapel (88625-47100, Aquapel) and reacting for 30 seconds until washed by Novec 7500 (9802122937, 3M). The channels were dried by air suction and kept in the oven at 65 °C until used.

Monodisperse microgel production.

Monodisperse microgels were produced as previously reported[21] or as follows. Two aqueous solutions were prepared: (i) 4 Arm-PEG VS MW 20,000 (PTE-200VS, NOF) at 8, 10, 20 and 24 % (w/v) in 0.3 M triethyloamine (TEOA) pH 8.25, pre-reacted with K-peptide (Ac-FKGGERCG-NH2), Q-peptide (Ac-NQEQVSPLGGERCG-NH2) at a final concentration of 250 µM and with RGD peptide (Ac-RGDSPGERCG-NH2) at a final concentration of 500 µM or 2.5mM and (ii) an 8mM di-cysteine modified Matrix Metallo-protease (MMP) (Ac-GCRDGPQGIWGQDRCG-NH2) (Genscript) or 3 mM, 9 mM or 10 mM poly(ethylene glycol) dithiol MW 1,000 (717142-1G, Sigma-Aldrich) pre-reacted with 10 µM Alexa-fluor 488 or 568-maleimide (Life Technologies). Please see the Table S1 for the composition according to MAP gel types. These pre-gel solutions were sterile-

filtered through a 0.2 μm Polyethersulfone (PES) membrane in a leur-lok syringe filter, injected into the microfluidic device and pinched off by oil phase (0.1% Pico-Surf in Novec 7500, SF-000149, Sphere Fluidics) (Fig. 3-1a). The flow rate for aqueous solutions was 0.6 ~ 2 mL/hr and for oil solutions was 6 ~ 10 mL/hr. Gels were collected from the device into a tube in oil phase, incubated overnight at room temperature in dark. Microgels in oil phase were vortexed with 20% 1H,1H,2H,2H-Perfluoro-1-octanol (PFO) (370533-25G, Sigma-Aldrich) in Novec 7500 for 10 seconds. Microgels were then mixed with 1:1 mixture of HEPES buffer (100 mM HEPES, 40 mM NaCl pH 7.4) and hexane followed by centrifugation at 10,000 rpm to separate microgels from oil for five times. Microgels were incubated in sterile-filtered 70% ethanol solution at 4 °C at least overnight for sterilization. Before *in vivo* or *in vitro* experiment, microgels were washed with HEPES buffer with 10 mM $CaCl_2$ for five times.

Polydisperse microgel production.

400 μL of pre-gel solution (5wt% 4-Arm PEG-VS with 4 mM of MMP-cleavable crosslinker) was injected into a 15 mL conical tube prefilled with 5 mL of heavy mineral oil (330760-1L, Sigma-Aldrich) with Span 80 (S6760-250ML, Sigma-Aldrich) at the concentration of 1%, 2%, 3% to generate droplets with different average diameters (Fig. 3-1b). The tube was rotated overnight using a Labquake Shaker (Barnstead Thermolyne). Microgels were then vortexed with HEPES buffer followed by centrifugation at 10,000 rpm five times to separate microgels from oil. Microgels were incubated in 70% ethanol solution at 4 °C at least overnight for sterilization.

Rheology techniques for measuring the storage modulus of MAP building blocks. We measured the storage modulus of an 8-mm disc gel using an Anton paar physica mcr 301 Rheometer. 40 µL of pre-gel solutions (20 µL of PEG with peptides, 20 µL of crosslinker) were pipetted onto sterile siliconized (Sigmacote; SL2-25ML, Sigma-Aldrich) slide glass, covered with another glass with 1mm spacer and incubated at 37 °C for two hours. Disc gels were swollen to equilibrium in PBS overnight before being measured. We performed an amplitude sweep (0.01-10% strain) to find the linear amplitude range for each. An amplitude within the linear range was chosen to run a frequency sweep (0.5-5 Hz). At least, four disc-gels were measure for each condition.

Diffusion measurement using photobleaching in MAP scaffold.

MAP gels were incubated with 100 µM 70 kDa dextran-FITC (FD70S-100MG, Sigma-Aldrich) solution in PBS or a 100 nM fluorescein solution in PBS. 20µL of microgels were pipetted and annealed in a 3 mm diameter PDMS well on a glass coverslip to form a MAP scaffold. Fluorescence recovery after photobleaching (FRAP) was conducted using a Leica TCS SP5 confocal microscope. A 20x dry objective and argon laser were used for bleaching and imaging. For pore diffusivity measurements, bleaching was performed with 30% laser power and 100% transmission, with imaging at 15% transmission to limit additional bleaching. For the single-phase bleaching measurements in non-porous hydrogel and PBS, 70% laser power and 100% transmission were used for bleaching, with 6% transmission used for imaging. After bleaching for 8 seconds, at least 50 images were taken with the interval of 390 ms (Fig. 3-4). A circle of 100 µm diameter centered on the bleach spot was taken as the analysis

region of interest (ROI) in all cases using ImageJ. The diffusivity was calculated via the approach of Soumpasis[44] (1):

$$D = \frac{.224w^2}{t_{1/2}} \quad (1)$$

where w is the ROI radius, $t_{1/2}$ is the halftime calculated by fitting the mean intensity of the ROI in time to an exponential equation (2):

$$F(t) = a + \frac{b}{2^{t/t_{1/2}}} \quad (2)$$

where a and b were obtained from the fitted curve.

Diffusion measurement in non-porous hydrogel using fluorescent intensity profile.

8-mm disc gels were prepared as previously described in the rheology technique section. Gels were swollen in PBS overnight and placed between two slide glasses in PBS with 100 µM 70 kDa dextran-FITC (FD70S-100MG, Sigma-Aldrich). The fluorescent images of gels (FITC) were taken every day and the intensity profiles over time were used to calculate the diffusivity using Fick's law.

Hydraulic conductivity measurement in the scaffold.

A custom-designed device was designed using Autodesk Inventor 3D CAD software, and printed in Watershed XC 11122 Normal-Resolution Stereolithography build in 0.004" layers from Proto Labs, Inc. (Fig. 3-5). For the MAP scaffold, 25 µL of microgel building blocks (5wt% crosslinked with MMP-cleavable dithiol) was casted on top of a 5 µm pore size cellulose membrane (SMWP01300, Fisher Scientific) in the bottom plane

of the device and annealed followed by the overnight incubation in PBS. For the non-porous scaffold, 10 µL of pre-gel solution (5 wt% PEG with 4 mM MMP-cleavable dithiol) was casted on top of the membrane in the device and incubated at 37 °C for two hours followed by the overnight incubation in PBS. Then 1 mL of PBS with blue food dye was injected into the device and the permeated volume over time was measured (Video S1 and S2). The hydraulic conductivity was calculated based on Darcy's law (3)[45]:

$$k = \frac{aL}{AT} \times ln\left(\frac{h_1}{h_2}\right) \quad (3)$$

where, a is the inner cross-sectional area of the graduated tube (cm^2), L is the test sample thickness (cm), A is the test sample cross-sectional area (cm^2). T is the time elapsed between the initial head and the final head (s), h_1 is the initial head across the test specimen (cm), and h_2 is the final head across the test specimen (cm).

Scaffold void fraction and pore size analysis.

Hydrogel particles of each type were injected into PDMS wells with 4-mm diameter and annealed followed by a z-stack confocal imaging spanning 250 µm in depth using the SP-5 confocal microscopy with 10x objective (Fig. 3-1d). To calculate the void fraction, 3D images were analyzed by statistical analysis of stacked images using ImageJ. To calculate the pore diameter distribution, 3D scaffold images were analyzed by a custom-developed Python-based software using the maximal ball algorithm[46,47] (Fig. 3-3a). Briefly, the code defines the pore as the diameter of a largest sphere found in a cavity or void by an inflating search. To organize the maximal spheres into pore-throat chains, groups of smaller inflated spheres were used to connect the maximal spheres. Along

the connection of smaller spheres, the connectivity of the maximal spheres was assembled to create a pore network (Fig. 3-3b).

Chapter 4. Stem Cell Behaviors in MAP Scaffold

4.1 Introduction

In this chapter, how MSC proliferation and retention can be enhanced by the interconnected pore network in MAP scaffolds. First, the *in vitro* behaviors of MSCs incorporated in MAP gels were compared to ones in MAP scaffolds with polydisperse hydrogel particles and non-porous hydrogels. In addition, MSC behavior *in vivo* was investigated using the subcutaneous murine implantation model.

4.2 Enhanced MSC proliferation *in vitro* in a microporous scaffold niche

MSCs incorporated in MAP scaffolds showed highly-interconnected and spread morphology through the void spaces between hydrogel building blocks (Fig. 3-3f). On the other hand, MSCs in non-porous gels possessed a round morphology with limited spreading and connection between cells. Although cells can degrade the hydrogel matrix locally to infiltrate, the time course for degradation prevents cells from migrating to occupy the space throughout the scaffold. In fact, multiple cells were confined in a small area (Fig. 3-3f inset).

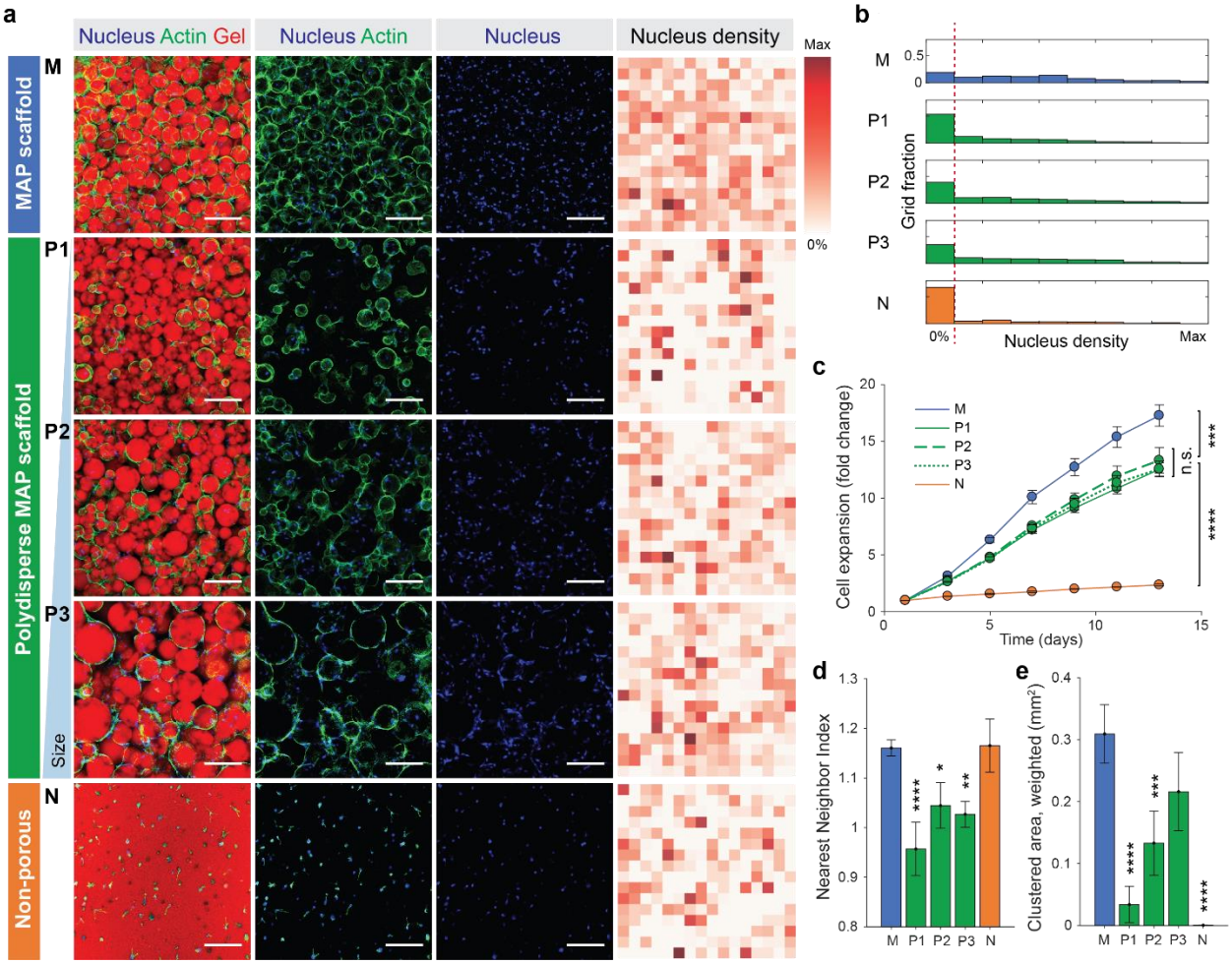

Figure 4-1 Controlled microporosity generated by monodisperse particles facilitates the highest cellular network formation and proliferation *in vitro*. **a** Fluorescent images of MSCs growing in monodisperse MAP scaffold (M), polydisperse MAP scaffold (P1, P2, and P3), and non-porous scaffold (N) following two weeks of *in vitro* culture. Corresponding heat map of nucleus density in the fields of view. The darker box indicates a region with a higher number of nuclei. (Blue, nucleus; Green, actin; Red, gel). Scale bar: 200 µm. **b** Histograms of nucleus density for five scaffold conditions (n = 4 scaffolds per condition). The red dashed line indicates the threshold for no nuclei in a region. **c** Cell proliferation of fluorescently transfected MSCs measured by increase in fluorescence intensity over time (n = 4). **d** Cell dispersity comparison based on spatial distribution of cells in the scaffold (n = 4, significance compared to M) **e** Cell connectivity comparison using the connectivity of actin in images (n = 4, significance compared to

M). All data are presented as average ± s.d. Statistical significance based on one-way ANOVA followed by Tukey's HSD *post hoc* test ($*p < 0.05$, $**p < 0.01$, $***p < 0.001$, $****p < 0.0001$); n.s. indicates not significant.

The ability to spread and migrate throughout the MAP scaffold led to more rapid proliferation, with increased void volume in MAP scaffolds leading to the highest proliferation rate. To correlate the microscale pore network with cell growth and proliferation, the intensity of red fluorescent protein (RFP) produced by RFP-transfected MSCs (RFP-MSCs) was measured for each scaffold over a two-week period. While the expansion of cells incorporated in non-porous gels yielded only a 2.3-fold increase, the expansion of RFP-MSCs in MAP scaffolds, including polydisperse ones, yielded at least a 12-fold increase (Fig. 4-1c). Among them, cells incorporated in mono-MAP scaffolds exhibited the highest cell proliferation, achieving a 17-fold increase in intensity, compared to any of scaffolds formed with polydisperse microgel building blocks. Enhanced proliferation was confirmed through the analysis of nucleus density, in which the lowest number of cell-free regions were observed in mono-MAP scaffolds (Fig. 4-1b). This implies that the highly controlled void network was ideal for inducing cell migration and growth in the scaffold, without any nutrient or space limitations. For poly-MAP scaffolds, reduction in performance may result from either small filled pores due to the presence of small particles or the reduction of volume for ingrowth due to the presence of larger hydrogel particles.

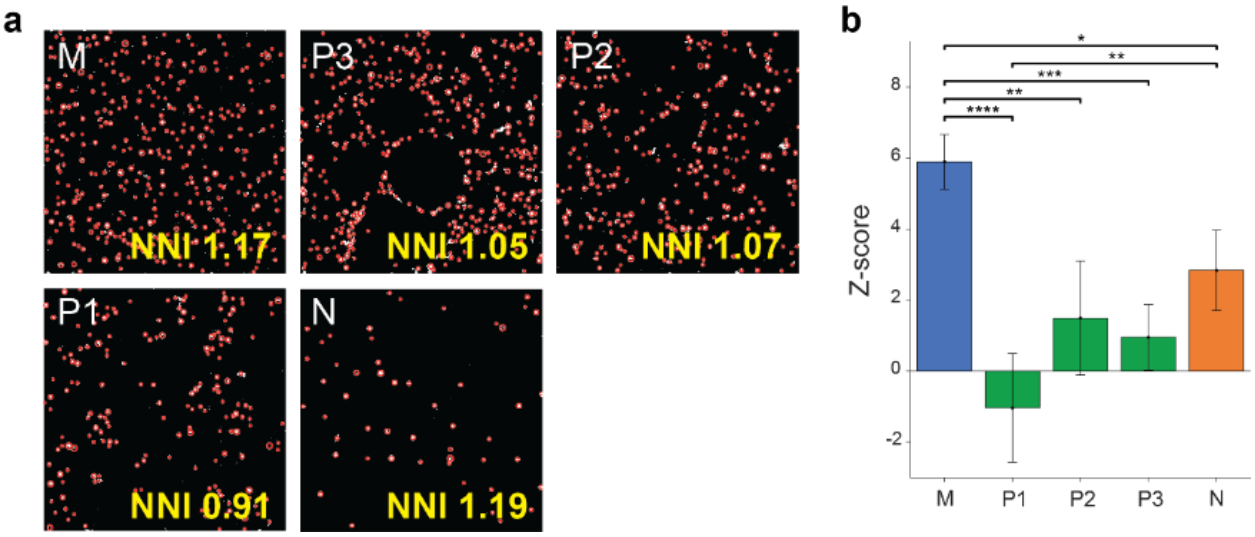

Figure 4-2 Analysis of cell dispersity using cell locations. **a** The location of cell nuclei was detected using DAPI images. The red dot indicates the location of the nucleus of each cell. The yellow text indicates the nearest neighbor index (NNI) of the scaffold analyzed. **b** Z-score value, a measure of statistical significance of rejecting the null hypothesis that the points are randomly distributed, was calculated based on the distances among cells in the scaffolds (n=4). Data are presented as average ± s.d. Statistical significance performed using one-way ANOVA followed by Tukey's HSD *post hoc* test ($*p$<0.05, $**p$<0.01, $***p$<0.001, $****p$<0.0001).

Cells growing in MAP scaffolds were more evenly dispersed than cells in poly-MAP scaffolds, which indicated the ability to migrate to fill in void spaces in a uniform manner. To evaluate migration throughout the scaffolds, cell dispersity was quantified using the locations of individual cell nuclei (Fig. 4-1d and Fig. 4-2a). The distance between each cell nucleus and its closest neighboring cell nucleus was used to calculate the nearest neighbor index (NNI), a measurement of the spatial distribution of objects that can quantify whether objects are regularly dispersed, randomly dispersed, or clustered[48]. In

poly-MAP scaffolds, a lower index was observed, indicating cells were more locally clustered, where cell migration presumably is hindered by small pores generated by a higher packing density of the smaller particles present in polydisperse gels that fill voids between larger particles. Non-porous scaffolds showed a comparable index with mono-MAP scaffolds mainly because of the uniform initial seeding of cells, and lack of cell migration. However, as discussed above there were far fewer cells than in MAP scaffold, thus producing a significantly lower Z-score (Fig. 4-2b). Moreover, the NNI for the non-porous scaffold did not accurately reflect clusters of cells in a very small area that are often present because the magnification used could not distinguish cells in a small confined area, such as ones in Fig. 2-4f.

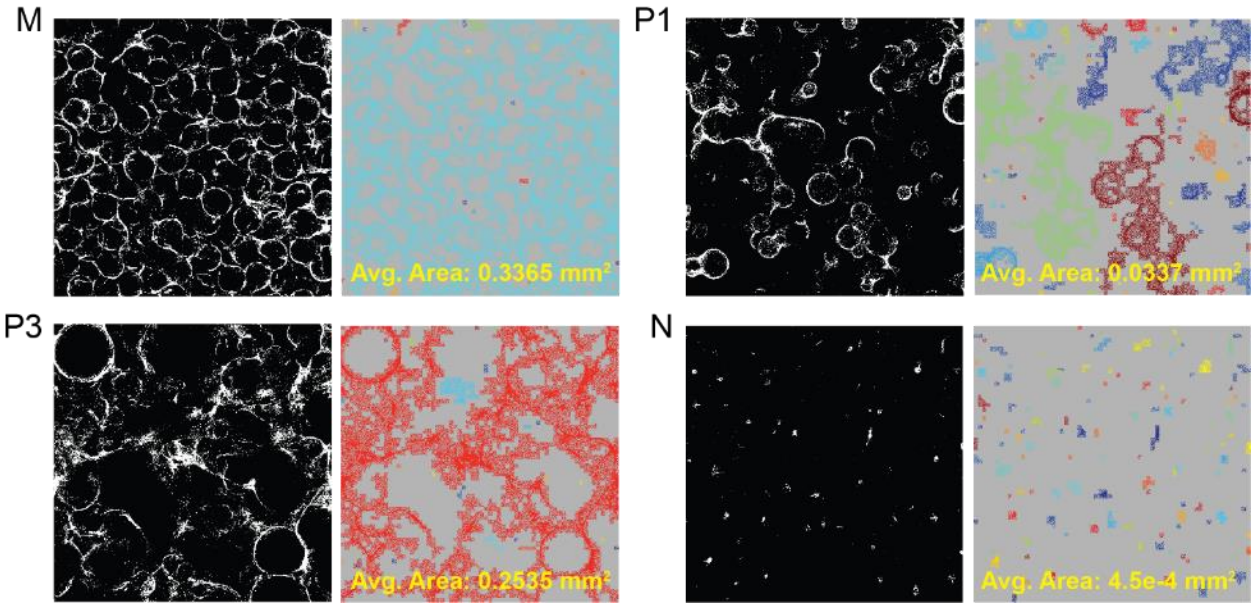

Figure 4-3 Analysis of cell connectivity using actin images. (Left: actin, right: connected actin indicated by same colors) **M**, MAP scaffold. **P1**, polydisperse MAP scaffold 1. **P3**, polydisperse MAP scaffold 3. **NP**, Nonporous scaffold. The yellow text indicates the average area of connected actin in each scaffold analyzed.

In addition to uniform dispersion, connectivity between cells was enhanced in mono-MAP scaffolds when compared to any other scaffolds, resulting in the largest area of connected actin. Cell connectivity and mechanical linkage was investigated using images of fluorescently-labeled actin as the cell-cell junctional complexes are associated with the actin cytoskeleton[49] (Fig. 4-1e and Fig. 4-3). In non-porous scaffolds, cells were isolated and confined, resulting in the lowest-connected actin area. Among poly-MAP scaffolds, the P3 scaffold showed the highest connectivity due to its larger pore diameter compared to that of P1 and P2 scaffold. However, the connectivity of P3 was still lower than mono-MAP scaffolds due to its non-uniform pore spaces. This indicates that the pore network in mono-MAP scaffolds provides a more ideal structure for maximizing connectivity between cells, which can enhance positive survival signals needed for cell viability and function[50,51].

4.3 Enhanced MSC retention *in vivo* in a microporous scaffold niche

Building off of our *in vitro* results and *in vivo* results without delivered cells (Fig. 2-2), we hypothesized that MAP scaffolds would enhance the retention of MSCs when compared with PBS or non-porous scaffolds *in vivo* (Fig. 4-4). MSCs producing RFP were injected into C57BL/6 mice, an immunocompetent strain, to recapitulate MSC survival in the presence of a functional immune system, and the fluorescent intensity was measured over a two-week period. RFP fluorescence intensity remained the highest for cells co-

delivered in MAP scaffolds compared to PBS and non-porous scaffold at the end of two weeks. Likewise, the cell area, which was defined by the area above a radiant efficiency of $2x10^7$, was also significantly higher in MAP scaffolds. Combined, these results support the formation of a microporous scaffold *in situ* that promotes cell proliferation and survival *in vivo*, perhaps due to enhanced transport, cell distribution and connectivity throughout the scaffold, as identified *in vitro*.

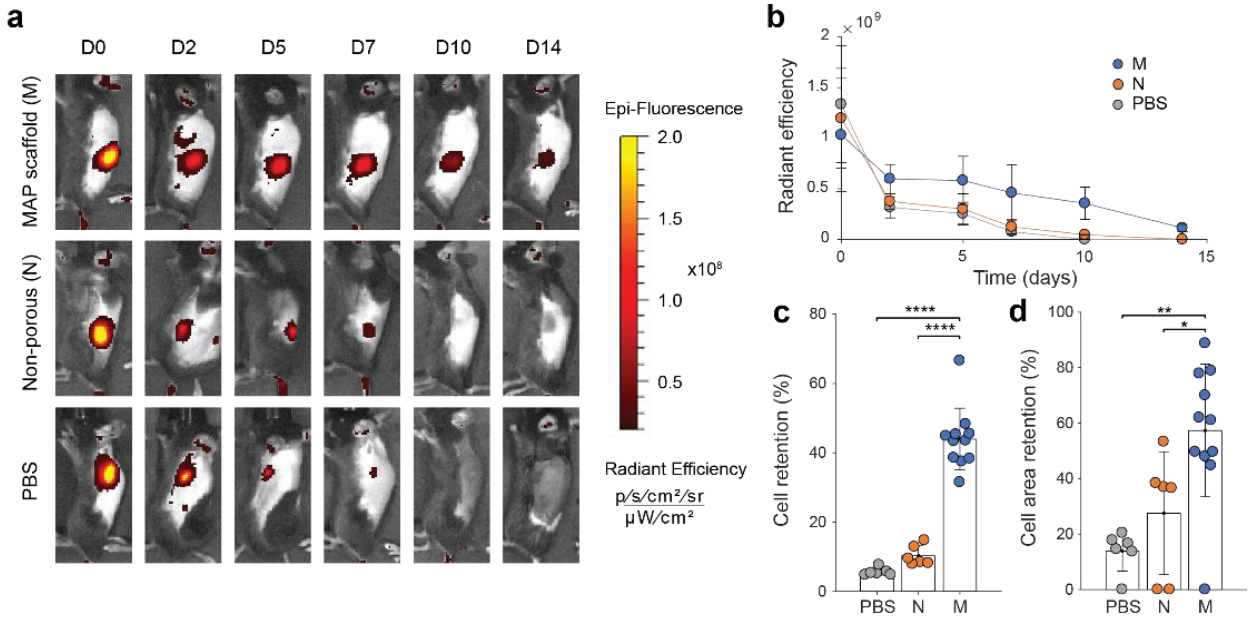

Figure 4-4 MSC retention after subcutaneous injection with MAP gel, non-porous gel, and PBS. **a** Representative fluorescence IVIS images of MSCs producing RFP that were subcutaneously injected into C57BL/6 mice with MAP scaffold (M), non-porous scaffold (N) and PBS at 0, 2, 5, 7, 10, 14 days post-implantation. **b** Integrated fluorescent intensity at each time point (*n* = 6-11). **c** Comparison of cell retention at day 7 relative to day 0. **d** Comparison of cell area at day 7 relative to day 0. Cell area was defined as an area with radiant efficiency higher than $2×10^7$. (**c, d**) Each point represents an individual mouse. All data are presented as average ± s.d. Statistical

significance based on one-way ANOVA followed by Tukey's HSD *post hoc* test ($*p < 0.05$, $**p < 0.01$, $***p < 0.001$, $****p < 0.0001$).

4.4 Methods

Mesenchymal stem cell culture on flask.

Strain C57BL/6 Mouse Mesenchymal Stem Cells with RFP (MUBMX-01201, Cyagen Biosciences) and strain C57BL/6 Mouse Mesenchymal Stem Cells with GFP (MUBMX-01101, Cyagen Biosciences) were maintained in Mouse Mesenchymal Stem Cell Growth Medium (MUXMX-90011, Cyagen Biosciences) according to manufacturer's specifications to retain stemness. Cells between passages 4-6 were used. Cells were maintained at lower than 80% confluency in culture.

Mesenchymal stem cell in vitro culture on the MAP scaffold.

MSCs labelled with RFP (MUBMX-01201, Cyagen Biosciences) were dissociated by trypsin and centrifuged down to remove medium. 60 µL of MAP in HEPES-buffered saline (pH 7.4) containing FXIII (10 U/mL) and 10 mM $CaCl_2$ was combined as mixed thoroughly with 60 µL of MAP microgel building blocks in HEPES-buffered saline (pH 7.4) containing thrombin (2 U/mL) with a positive displacement pipette (MICROMAN, Gilson, Inc.). Cells were resuspended and spiked in MAP building blocks at 1,000 cells/µl concentration. These MAP gels were kept on ice to prevent annealing as well as maintaining the MSC viability. 20 µL of MAP gels with MSCs at 1,000 cells/µL was pipetted into silicone isolators (GBL664206-25EA, Sigma-Aldrich) in a tissue culture

plate (08-772-50, Thermo Fisher Scientific) and incubated for 90 mins at 37 °C followed by adding a complete cell culture medium. Cells were grown in 5 % CO_2 and 37 °C and 1 mL of medium was changed every 3-4 days. The fluorescent intensity from RFP was detected using a plate-reader (BioTek Cytation5). In each sample, at least 6 points of RFP intensity were measured (Ex: 545, Em: 605) using the area scanning function. At day 14, samples were gently washed with PBS twice, fixed with 4% PFA overnight at 4 °C followed by Hoechst (1/500) (Thermo Fisher Scientific) and phalloidin 647 (1/500) (Thermo Fisher Scientific) staining at room temperature for 4 hours. Then the scaffolds were gently washed twice with PBS and kept at 4 °C until imaged.

Mesenchymal stem cell in vitro culture on the non-porous scaffold.

PEG-VS scaffolds (5wt% r=0.8 MMP-1 crosslinker, 250 µM K, 250 µM Q, 500 µM RGD) were used to encapsulate MSCs (1,000 cells/µL). Gels were formed for 15 minutes (TEOA 0.3M, pH 8.25) before being placed into appropriate media. The fluorescent intensity detection and staining was performed as for MAP scaffold *in vitro* experiments.

Cell dispersity and connectivity analysis.

To determine cell dispersity and connectivity in scaffolds, 4 samples per each condition were investigated. 13 z-slices were taken in each gel, spanning 1.16 mm x 1.16 mm in x and y and 50 µm in z using Leica SP8 with 10x/0.30 DRY lens. For dispersity analysis, the DAPI channel of these images were used to locate cells in the scaffolds and determine the distance between cells and calculate the nearest neighbor index (NNI), the ratio of the observed average distance between nearest neighbors to the expected

average for a hypothetical random distribution[48] using a custom-developed MATLAB code (Fig. 4-2):

$$NNI = \frac{d_{obs}}{d_{exp}} = \frac{d_{obs}}{0.5 \times \sqrt{\frac{a}{n}}} \quad (4)$$

where d_{obs} is the mean observed nearest neighbor distance, d_{exp} is the expected average for a hypothetical random distribution, a is the area of the scaffold, and n is the number of cells.

For connectivity analysis, actin images were used to calculate the weighted average area of interconnected actin islands using a custom-developed MATLAB code (Fig. 4-3).

In Vivo Imaging System (IVIS).

Strain C57BL/6J mice (The Jackson Laboratory) were anesthetized using continuous application of aerosolized isofluorane (3 vol%) throughout the duration of the procedure. 60 µL of MAP in HEPES-buffered saline (pH 7.4) containing FXIII (10 U/mL) and 10 mM CaCl2 was combined as mixed thoroughly with 60 µL of MAP building blocks in HEPES-buffered saline (pH 7.4) containing thrombin (2 U/mL) with a positive displacement pipette (MICROMAN, Gilson, Inc.). 100 µL of MAP building blocks with one million MSCs expressing RFP (MUBMX-01201, Cyagen Biosciences) was injected subcutaneously into mice via 25-gauge needles. As controls, 100 µL of PBS with one million MSCs expressing RFP and 40 µL of pre-gel solution (5wt% PEG with 4mM MMP-cleavable dithiol, swelling ratio 2.5) with one million MSCs expressing RFP were injected using the same method. Two injection sites on opposing sides of the back per mouse were used to avoid potential signal overlap during imaging. To monitor cell

viability and distribution, the RFP fluorescence was measured using a Perkin Elmer IVIS Lumina II on days 0, 2, 5, 7, 10, 14. Before imaging, mice were anesthetized with 3% isofluorane/air. For each image acquisition, a gray scale body surface image was collected, followed by an overlay of the fluorescent (Ex: 535, Em: 600) and their radiant efficiency were quantified using Living Image software (Caliper LifeSciences). All animal experiments were performed according to established animal protocols.

Chapter 5. MSC activity modulation by biochemical and biophysical properties

5.1 Introduction

MAP scaffolds provide an independent control of biophysical properties from porosity. In this chapter, three representative physical properties are modulated that affect stem cell behavior and activity: stiffness, biding motif concentration and degradability. The effect of these properties on the level of stem cell activities *in vitro* and *in vivo* was investigated.

5.2 Independent modulation of MAP scaffolds

In addition to controlling microporosity using monodisperse microgel building blocks in the previous chapter, we hypothesized that the function of MSCs in the injected scaffold could be controlled through modulation of material properties of the building blocks, such as degradability, stiffness, and cell-binding motif amount[17,52,53]. Specifically, we were interested in maintaining viable cells that retain an MSC phenotype to extend cell-based therapies[14,54–56]. To arrive at a final set of microgel precursors for *in vivo* experiments, different weight percent, stoichiometry, crosslinker types and cell binding motif (RGD) concentrations were screened (Fig. 4a, Table 1). Two soft building blocks were designed to have storage moduli of 500 Pa with enzymatically-degradable (SoD1) and non-degradable (SoN1) crosslinkers and a standard RGD concentration (0.5 mM)

to isolate the effect of MMP-triggered degradability. Stiff building blocks were designed using the non-degradable formulation, decoupling degradability from stiffness. We avoided simultaneous modulation of stiffness with MMP-degradable crosslinkers since we observed that stiffness and degradability were difficult to independently control. For example, doubling the crosslinking concentration of degradable crosslinkers resulted in higher stiffness but also resulted in a significant loss of degradability (Fig. 5-1a). In fact, the degree of cell spreading through local degradation is reduced for cells encapsulated in 10wt% degradable gel (Fig. 5-1b), which contrasts with increasing spread cell morphology on a stiffer 2D substrate[57].

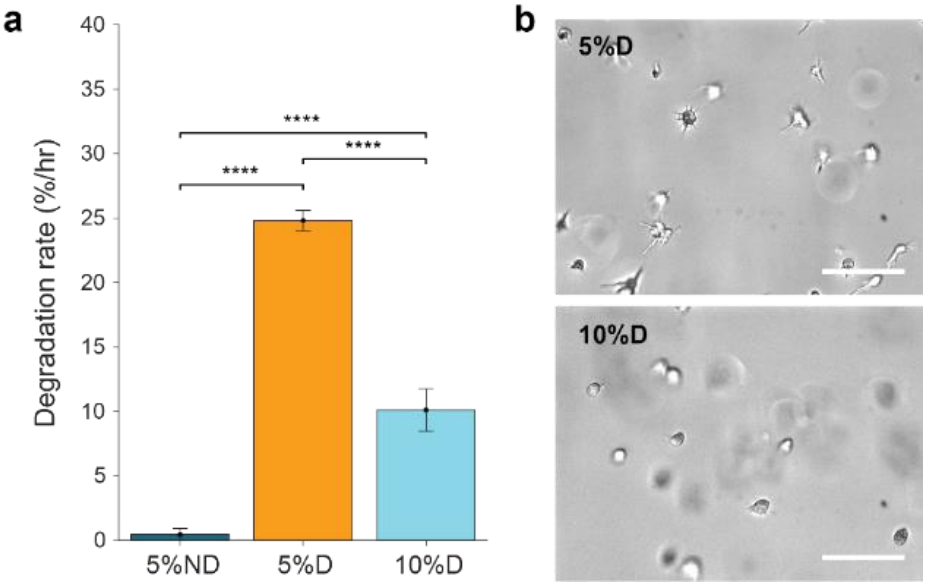

Figure 5-1 Correlation between crosslinking density and degradability. **a** Degradation rate of 5wt% non-degradable gels (5%ND), 5wt% MMP-degradable gels (5%D) and 10wt% MMP-degradable gels (10%D) in 1% TriPLE in PBS at 37°C (n = 3). Data are presented as average ± s.d. Statistical significance performed using one-way ANOVA followed by Tukey's HSD *post hoc* test (∗∗∗∗p < 0.0001). **b** Bright field images of *in vitro*

MSC culture at day 4 in MMP-degradable non-porous gels with 5wt% and 10wt% PEG concentration. Scale bar: 100 μm.

In our system, the crosslinking density of the stiffer microgel building blocks was increased to achieve a storage modulus of 2,500 Pa while maintaining RGD concentration (StN1) such that the effect of stiffness could be investigated independently from degradability or adhesive ligand concentration. Importantly, due to *in situ* assembly of cells into micropores formed within the annealed MAP scaffolds, increasing the stiffness of hydrogel building blocks did not result in changes in confinement of cells. To investigate the effect of cell binding motif concentration, the RGD concentration within the stiff non-enzymatically-degradable hydrogel formulation was increased five-fold (StN5), without changing the storage modulus (Fig. 5-2a). Although these four distinctive compositions (SoD1, SoN1, StN1, StN5, Fig. 4a) had different swelling ratios in an aqueous buffer, we used microfluidic droplet generation to tune the pre-swollen building block size, such that each microgel type was similar in size after swelling (Fig. 5-2b). This was important to preserve the microporous structure of the MAP scaffolds and decouple potential effects of material properties from microporosity. By manufacturing microgel particles with well-controlled material properties we could create MAP scaffolds with orthogonally-controlled properties to study the effect of microenvironmental cues on stem cells.

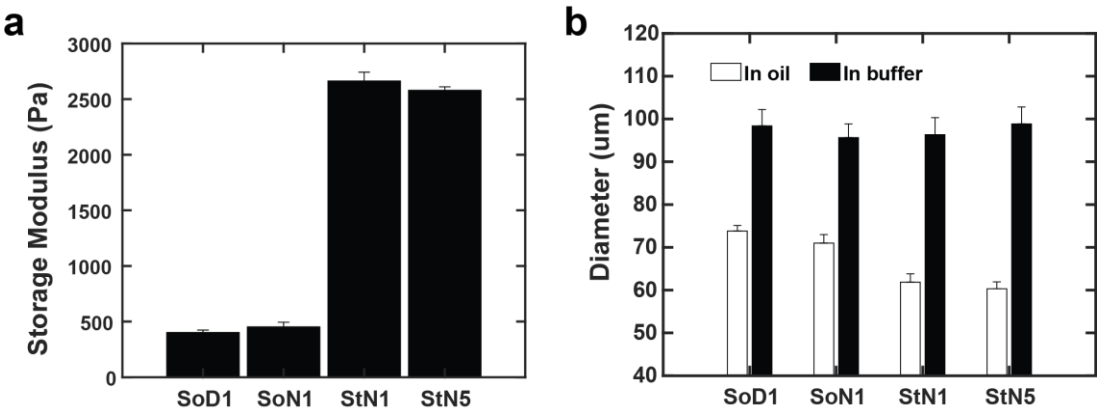

Figure 5-2 Independent modulation of physical properties of building blocks. **a** Storage modulus of each µgel type measured by rheometer. Two distinct storage moduli were achieved regardless of degradability or RGD concentration (*n*=4). **b** Diameter of each µgels in oil phase and in water (buffer) phase. Microfluidic fine-tuning of droplet diameter in oil phase produced 100 µm highly monodisperse particles after swelling regardless of gel composition. All data presented as average ± s.d.

Table 1 The composition of MAP gels

Building block type	**4-Arm PEG-VS concentration [w/v]**	**Crosslinker concentration**	**Crosslinker type**	**RGD concentration**
SoD1	5wt%	4mM	MMP cleavable	0.5mM
SoN1	4wt%	3mM	Non-degradable	0.5mM
StN1	10wt%	9mM	Non-degradable	0.5mM
StN5	12wt%	10mM	Non-degradable	2.5mM

5.3 MSC behavior modulation *in vitro*

All three material properties that we modulated affected *in vitro* MSC proliferation. SoD1 showed a higher expansion rate than SoN1, indicating that material degradability plays a role when material stiffness is low (Fig. 5-3b). In degradable materials, cells can locally create new nanoscale pores, presumably revealing more RGD binding sites which drives growth. The significantly larger actin spread area in SoD1 compared to SoN1 supports this mechanism (Fig. 5-3e, f). Stiff gel building blocks also led to higher proliferation, which is in agreement with previous work that indicated that MSCs spread more and proliferate more readily on stiffer 2D substrates[58,59]. MSC expansion was further enhanced on these stiff scaffolds by incorporating higher RGD concentration. For the enzymatically-non-degradable gel conditions, more RGD sites on the surface may be beneficial to promote growth as cells have more difficulty in degrading and revealing new RGD binding sites. In fact, StN5 was observed to promote slightly larger actin spread area per cell than StN1, indicating that the high RGD enhanced binding of cells to the substrate and spreading (Fig. 5-3e, f).

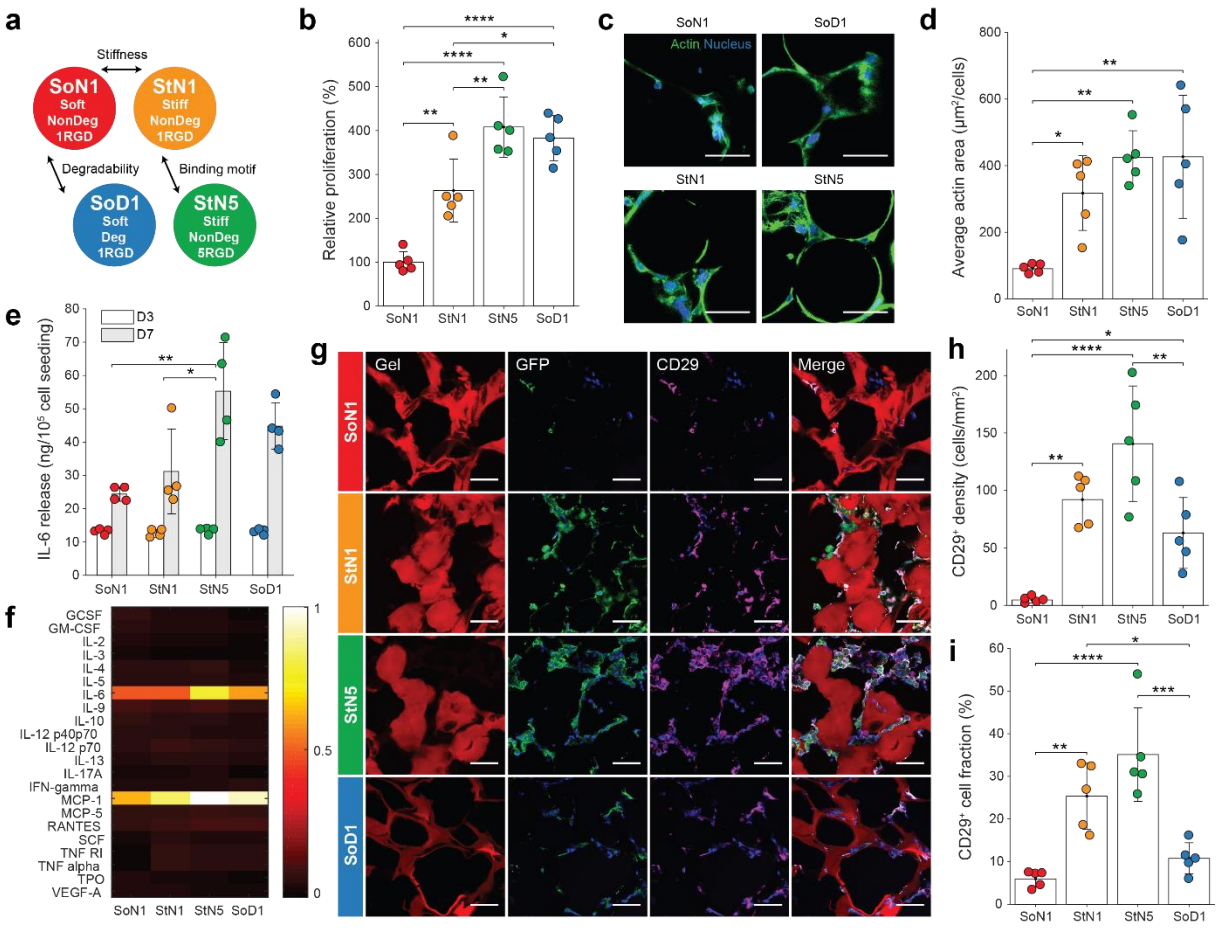

Figure 5-3 Modulating MAP scaffold material properties affect MSC function. **a** Four MAP gel formulations to study the effect of degradability, stiffness and binding motif concentration. **b** Relative cell expansion *in vitro* at 7 days (*n* = 5). **c** Representative fluorescent images of MSC growth *in vitro* following two weeks (Blue, nucleus; Green, actin). Scale bar: 50 μm. **d** Average actin area normalized by the number of cells for *in vitro* culture (*n* = 5). **e** The cumulative release of IL-6 *in vitro* at day 3 and day 7 (*n* = 4). **f** Relative comparison of cytokine release *in vitro* at day 7 normalized by the maximum release (*n* = 4). **g** Representative fluorescent images of GFP-producing MSCs in MAP scaffolds subcutaneously injected into C57BL/6 mice following two weeks (Red, gel; Blue, nucleus; Green, GFP; Magenta, CD29). Scale bar: 50 μm. **h** $CD29^+$ cells per area in scaffolds at week 2 (*n* = 5). **i** Ratio of CD29+ cells to all cells in the scaffolds at week 2 (*n* = 5). (**h, i**) Each dot in the plots represents an individual mouse. All data are

presented as average ± s.d. Statistical significance based on one-way ANOVA followed by Tukey's HSD *post hoc* test ($*p < 0.05$, $**p < 0.01$, $***p < 0.001$, $****p < 0.0001$).

We next examined whether this increased MSC proliferation was accompanied by enhanced function of MSCs. MSCs are known to produce many cytokines and growth factors, such as IL-6, a factor potentially linked to therapeutic function of MSCs[9]. IL-6 was measured in cell culture media at day 3 and 7 (Fig. 5-3c). At day 7, MSCs seeded in StN5 scaffolds secreted significantly higher levels of IL-6 than cells grown in SoN1 and StN1 starting with the same cell seeding population, reflecting the higher cell proliferation in StN5. We then investigated a larger panel of cytokines release from MSCs in culture media at day 7. The dominant cytokines among the panel were IL-6 and MCP-1 regardless of gel types, which correspond to the secretome of undifferentiated MSCs *in vitro*[54,60]. In agreement with our previous results, MSCs seeded within StN5 demonstrated the highest levels of IL-6 and MCP-1 (Fig. 5-4), either reflecting higher proliferation or improved function. Importantly, these findings also indicate that the stiffer material did not lead to changes in cellular phenotype that would lead to loss of therapeutic cytokine secretion.

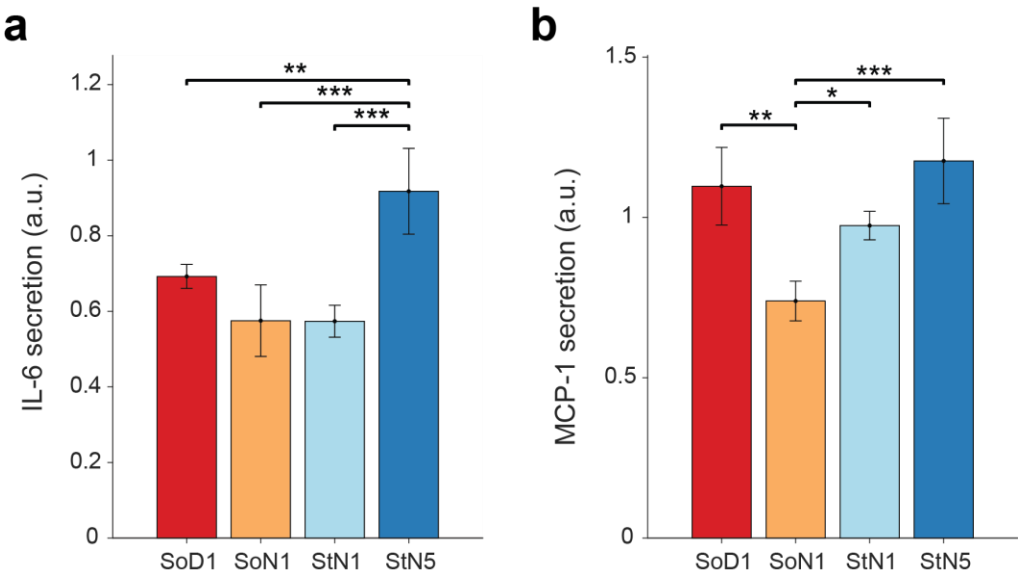

Figure 5-4 Relative comparison of two major cytokines produced *in vitro* from MSCs at day 7 measured by cytokine protein array. **a** IL-6 (n = 4). **b** MCP-1 (n = 4). Data are presented as average ± s.d. Statistical significance performed using one-way ANOVA followed by Tukey's HSD *post hoc* test ($*p < 0.05$, $**p < 0.01$, $***p < 0.001$).

5.4 MSC behavior modulation *in vivo*

To investigate the *in vivo* response to the four types of MAP scaffolds, MSCs expressing GFP were subcutaneously injected in C57BL/6 mice along with the microgel building blocks and scaffolds were excised two weeks after implantation. In all MAP scaffolds, injected MSCs were identified by the colocalization of CD29 and GFP (Fig. 5-3g) and negative staining for CD11b (Fig. 5-5b). The number of cells with CD29 staining in the scaffold were counted to calculate the stem cell density and fraction (Fig. 5-6). The density of $CD29^+$ cells was the highest in StN5 scaffolds (Fig. 5-3h), corresponding

to the results of our *in vitro* cell proliferation experiments. The lower *in vivo* preservation of MSCs in SoD1, degradable gels, than *in vitro* may be due to the degradable formulation losing physical integrity more rapidly once implanted and exposed to proteases. Stiffer gels also resulted in $CD29^{+}$ cells occupying a larger fraction of the total cells present in scaffolds (Fig. 5-3i). Overall, the stiffer gels with higher RGD (StN5) retained the implanted stem cell population at two-fold higher levels compared to our original formulation (SoD1).

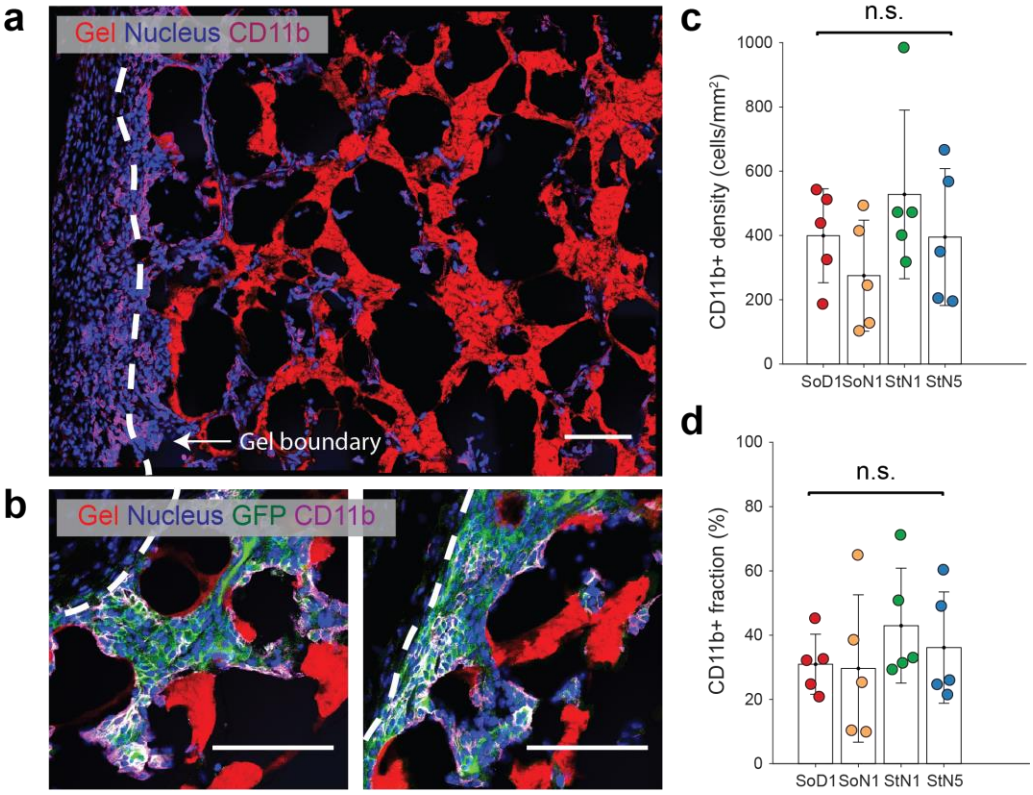

Figure 5-5 Immune response to the scaffolds. **a** Representative image of immune cell staining (CD11b) near the periphery of the StN5 scaffold in day 14. Scale bar: 100 µm. **b** Zoomed-in images of $CD11b^{+}$ cells near the scaffold. (**a, b**) Dotted line: the boundary between scaffold and tissue. Scale bar: 100 µm. **c** Number of $CD11b^{+}$ cells per area in

the periphery of the scaffolds (*n* = 5). **d** Ratio of CD11b+ cells in the periphery of the scaffolds (*n* = 5). (**c, d**) Each dot in the plots represents an individual mouse. All data presented as average ± s.d. Statistical significance performed using one-way ANOVA followed by Tukey's HSD *post hoc* test; n.s. indicates not significant.

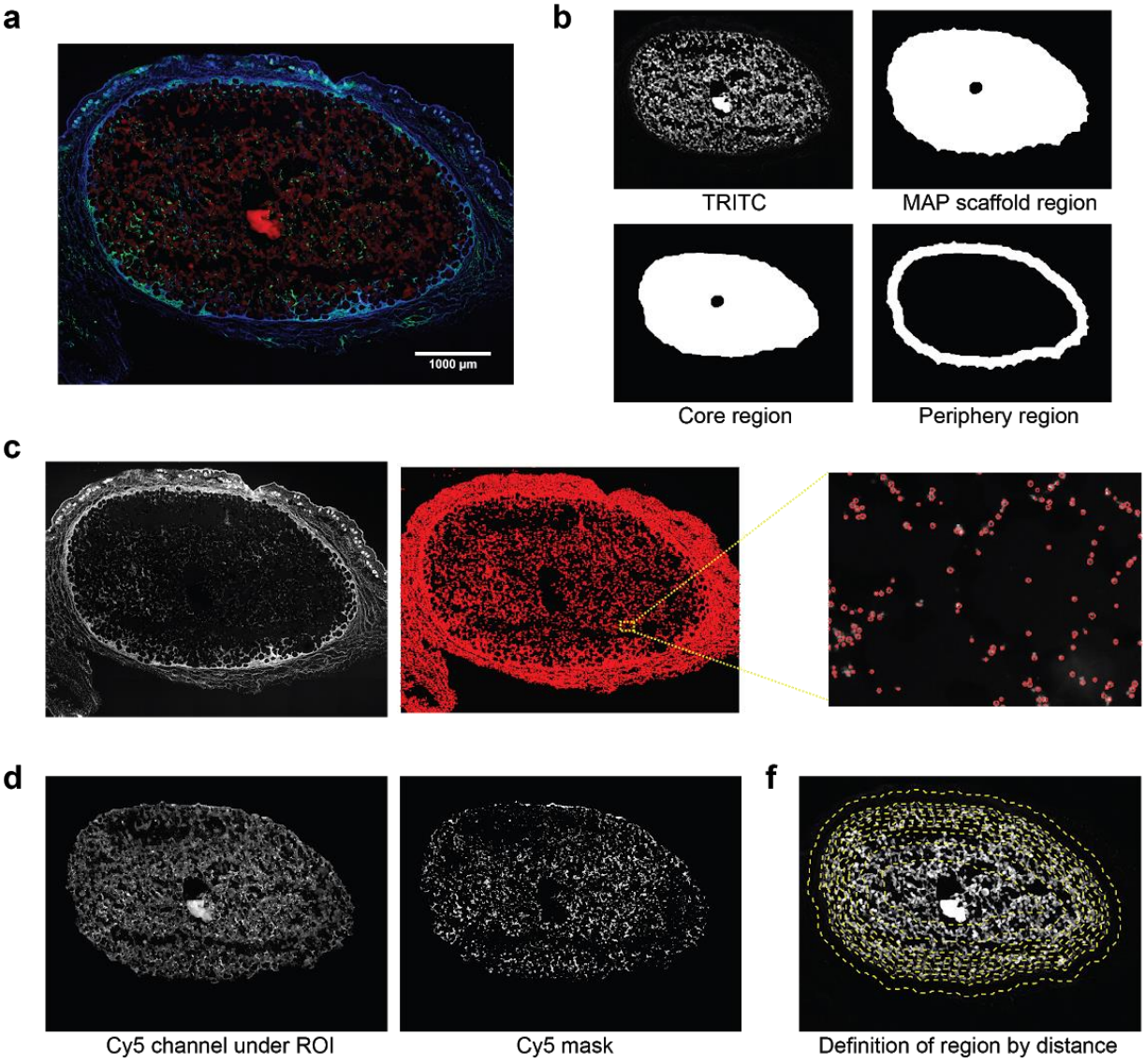

Figure 5-6 Analysis of *in vivo* tissue images. **a** Example of tissue images at day 14 (Blue, nucleus; Green, GFP; Cy5, CD29; Red, gel). Scale bar: 1 mm. **b** Defining the region of interest (ROI) using the TRITC channel (gel) image. The core region was defined as 200 µm interior from the boundary and the periphery was defined as the remaining area. **c** Cell number counting using DAPI images. Red dots represent the locations of cells. **d** Definition of the region of protein expression using the Cy5 channel. Background signal was removed by the threshold. **e** Definition of the region by distance. The outermost region is the region 200 µm outside of the scaffold. The region inside the scaffold was divided into concentric layers every 100 µm for 500 µm and then 200 µm,

300 μm and 500 μm as shown in the figure to calculate the cell density as a function of the distance from the interface.

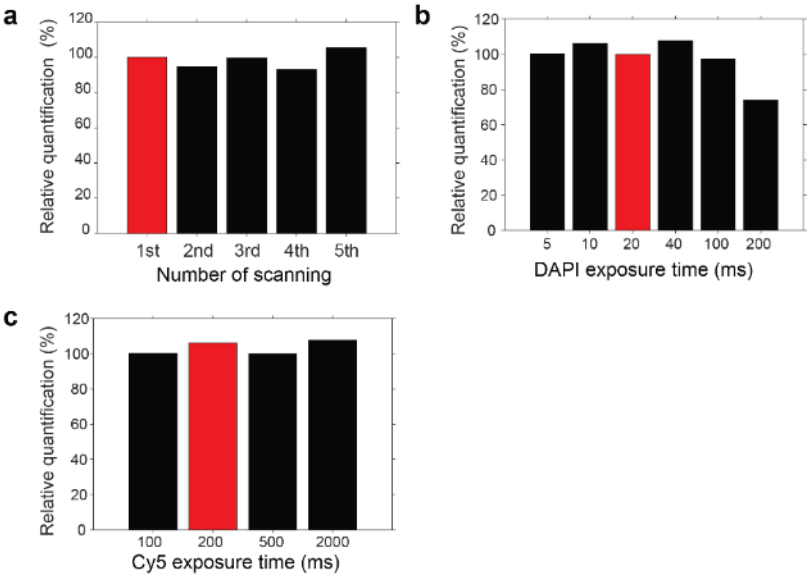

Figure 5-7 CD29^{+} cell quantification by imaging conditions. **a** Quantification by the number of scanning times. **b** Quantification by the exposure time of the DAPI channel. **c** Quantification by the exposure time of the Cy5 channel. All values were normalized to the value of the red bar, the standard imaging condition for the whole analysis.

Table 2 Antibody information

Antibody	Type	Manufacturer	Cat #	Dilution Factor
Chicken anti GFP	Primary	Abcam	#ab13970	1:500
Rat anti mouse Integrin beta 1	Primary	Abcam	#ab95623	1:200
Rat anti mouse CD31	Primary	Abcam	#ab7388	1:200

Rat anti mouse CD11b	Primary	BD Biosciences	#553308	1:200
Goat anti Rat IgG AF 647	Secondary	Thermo Fisher	#A-21247	1:200
Goat anti Chicken IgY AF 488	Secondary	Thermo Fisher	#A-11039	1:200

5.5 Tissue ingrowth and vascularization into the MSC-containing MAP scaffolds

Microporosity of the implanted MSC-containing MAP scaffolds also induced cell migration, in-growth of host tissue, and vascularization important for improved clinical function. The integration of the MAP scaffolds was evaluated by the number of cells near the boundary between the surrounding tissue and MAP scaffold (Fig. 5-8a, b and Fig. 5-6f). The density of cells within a 200 µm region outside of and neighboring the scaffold was about 1,580 cells/mm^2. Within a region ~100 µm deep into the scaffold boundary, the cell density was similar to the surrounding tissue, indicating that all four types of MAP scaffolds integrated well with the tissue. Cell density gradually decreased in all MAP scaffolds up to a distance of 1.5 mm, with SoN1 showing the lowest cell density in the scaffold core. The other formulations remained cellular (~ 500 cells/mm^2) throughout the scaffold, even at depths of 1.5 mm from the implant interface. This value is above the initial seeding density (~ 125 cells/mm^2 given that the tissue sectioning was ~25 µm in thickness). Since MSC retention cannot account for the increase in cell

numbers, this indicates that MAP scaffolds induced the migration of endogenous cells deep into the scaffold and maintained these cells over weeks overcoming transport limitations of conventional hydrogels. The SoD1 formulation resulted in a greater number of cells in the periphery of the scaffold, suggesting more cell migration and tissue ingrowth into the scaffold corresponding to scaffold degradation over time.

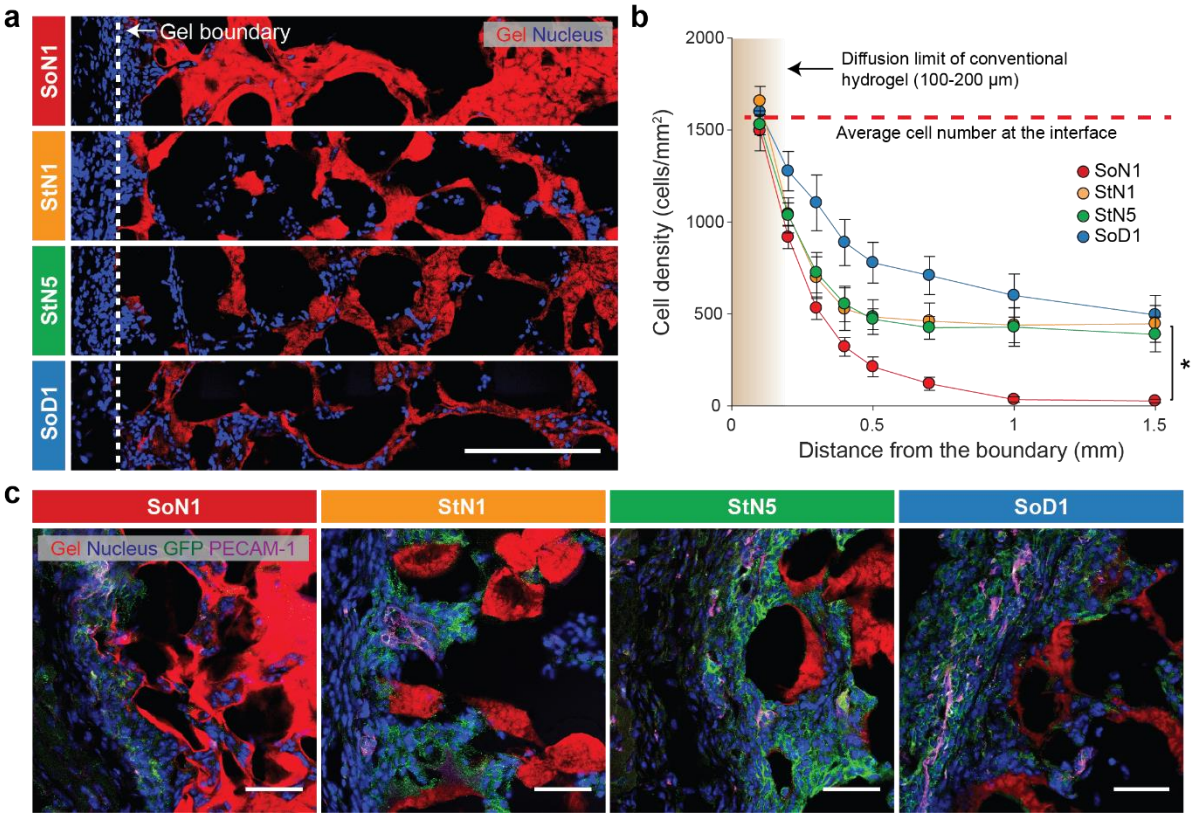

Figure 5-8 Tissue ingrowth and vascularization into microparticle scaffolds. **a** Representative images of tissue slices following two weeks of implantation of MSCs with materials shown in Fig. 4a. The dotted line indicates a boundary with the surrounding tissue. Scale bar: 200 μm. **b** Number of cells per area as a function of the distance from the interface between the MAP scaffold and the tissue (n = 5). Data presented as average ± s.e.m. Statistical significance performed using one-way ANOVA with a Dunnett *post hoc* multiple comparison test (*p < 0.05). **c** Representative images

of platelet endothelial cell adhesion molecule (PECAM-1) and GFP immunostaining near the boundary of the scaffolds following two weeks indicating the presence of implanted GFP-MSCs and endothelial cells growing in from surrounding tissue. Scale bar: 50 µm.

Endothelial cell markers (PECAM-1) were found within the periphery of all four types of MAP scaffolds, providing evidence of vascularization (Fig. 5-8c). This corresponds to our earlier experiment demonstrating that vascularization was facilitated through the presence of pores within the scaffolds which helped with larger scale cellular sheet migration deep into the scaffolds, which is not apparent in non-porous scaffolds after two weeks (Fig. 2-2). Aspects of the immune response to the different scaffolds was also evaluated. Since myeloid cells, including neutrophils and monocytes, are the first to infiltrate an implanted biomaterial[61], we examined the myeloid cell response to our MSC-containing MAP scaffolds. Most of the myeloid cells analyzed ($CD11b^+$) were located at the periphery of the scaffolds (Fig. 5-5a). The quantification of $CD11b^+$ cell density and fraction were not significantly different among MAP scaffolds (Fig. 5-5c, d), indicating that the innate immune response was not significantly different across the MAP scaffolds.

5.6 Methods

Gel degradation experiment.

10 µL of pre-gel solutions (5 µL of PEG with peptides, 5 µL of crosslinker pre-reacted with 10 µM Alexa-fluor 488-maleimide) were pipetted onto sterile siliconized (Sigmacote; SL2-25ML, Sigma-Aldrich) slide glass, covered with another glass with 1mm spacer and incubated at 37°C for two hours. The final concentrations of PEG and crosslinkers were 5wt% 4-Arm PEG-VS with 4 mM PEG-dithiol (5%ND), 5wt% 4-Arm PEG-VS with 4 mM MMP-cleavable dithiol (5%D) and 10wt% 4-Arm PEG-VS with 8mM MMP-cleavable dithiol (10%D). Gels were swollen to equilibrium in PBS overnight before being transferred to a 24-well insert with fluorescent-blocking membrane (08-772-147, Fisher Scientific); one gel per a well. The insert was inserted into a 24 well-plate with 1 mL of 1% TryPLE (12604013, Gibco) in PBS. The fluorescent level at the bottom of the plate was measured by the plate-reader (BioTek Cytation5) at 37°C for 12 hrs.

IL-6 ELISA and cytokine arrays.

1 mL of supernatants of *in vitro* cell culture media in MAP scaffolds were collected at day 3 and day 7. The IL-6 level was detected using Mouse IL-6 ELISA Set (BD Biosciences, #550950) according to the manufacturer's manual. The plate was read using a plate-reader (BioTek Cytation5). The relative mouse cytokine level was detected using RayBio C-series Mouse Cytokine Antibody Array C1 (RayBiotech, AAM-CYT-1-8) according to the manufacturer's protocol. Conditioned medium samples were incubated with blocked membranes overnight at 4°C. Prepared membranes were imaged using MyECL Imager (#PI62236, Thermo Scientific). Scanned images were analyzed using

the ImageJ plug-in “Protein array analyzer” (written by G. Carpentier, 2010; http://rsb.info.nih.gov/ij/macros/toolsets/ Protein%20Array%20Analyzer.txt).

Subcutaneous MSC injection model.

Strain C57BL/6J mice (The Jackson Laboratory) were anesthetized using continuous application of aerosolized isofluorane (3 vol%) throughout the duration of the procedure. 60 µL of MAP in HEPES-buffered saline (pH 7.4) containing FXIII (10 U/mL) and 10 mM $CaCl_2$ was combined as mixed thoroughly with 60 µL of MAP building blocks in HEPES-buffered saline (pH 7.4) containing thrombin (2 U/mL) with a positive displacement pipette (MICROMAN, Gilson, Inc.). 2.4 µl of MSC suspension was then added and mixed thoroughly. 100 µL of MAP building blocks with MSC GFP (MUBMX-01101, Cyagen Biosciences) at 5,000 cells/µL was injected subcutaneously into mice via 25-gauge needles. Four injection sites on the back per mouse were used to accommodate all four test conditions (SoD1, SoN1, StN1 and StN5). Mice were sacrificed at week 2 and MAP scaffolds were excised and immediately fixed in 4% PFA for two hours before flash frozen in OCT compound (Tissue-Tek). These OCT tissue blocks were kept at -80 °C until sectioned at 25 µm thickness using cryostat (Leica CM1950) and collected onto 25 x 75 mm charged slides (1358W, Globe Scientific). Sections were dried at room temperature overnight and kept at -20 °C until stained. All animal experiments were performed according to established animal protocols.

Tissue section immunofluorescence.

Slides containing tissue sections were washed and blocked using 10% normal goat serum (50062Z, Invitrogen) for two hours at room temperature and then stained with primary antibodies overnight at 4 °C. Primary antibody dilutions were prepared as in the Table S2. Sections were incubated in secondary antibodies with 1/500 diluted Hoechst for 2 hours at room temperature, and subsequently washed with PBS. Secondary antibody dilutions were prepared as in the Table S2. Sections were mounted in Antifade Gold mounting medium (9071S, Cell Signaling Technology) and imaged using Leica Confocal SP-5 with 63x water immersion objective lens or Nikon Ti Eclipse with 10x objective lens.

Computational analysis of tissue images.

Images were analyzed using a MATLAB code. Briefly, the code defines the region of an injected MAP scaffold region using the TRITC channel. It divides the region into two: a periphery region of interest (ROI) (200 μm into and out of the scaffold) and core ROI (inside of the periphery region) (Fig. 5-6). For ROI regions, the code reads the Cy5 channel intensity profiles and defines regions of protein expression using a threshold (identical for all sample images). The ratio of cells with protein expression was calculated by the ratio of cells having a nuclear stain also in the protein expression region for each ROI. The density of cells was calculated by the total number of cells under the protein expression mask divided by the area of the ROI. The cell density as a function of the distance from the interface was calculated by counting the number of cells in a subregion of the scaffold that was divided by distance (Fig. 5-6f). We verified that the quantification by this method is insensitive to imaging conditions: exposure time

and number of scans, although we kept the imaging condition the same for all samples (Fig. 5-7). Tissue slice areas with physical defect from imperfect tissue sectioning were excluded manually in the analysis.

Statistical analysis.

All values are depicted as mean ± standard deviation unless stated. Statistical comparisons were performed using GraphPad Prism 8.0 or MATLAB version R2016b (MathWorks, Inc.). The significance between two groups was analyzed by a two-tailed Student *t*-test. The significance between multiple groups was analyzed by a one-way ANOVA. Values were considered to be significantly different when $p < 0.05$. Details for statistical analyses for each comparison are reported in Table S3.

Chapter 6. Localized Drug Delivery using MAP Scaffolds

6.1 Introduction

Drugs can be loaded and released from MAP scaffolds to modulate the behavior of endogenous cells or injected cells. Hydrogels, the body component of MAP gels, can provide temporal control over the release of various therapeutic agents, including small-molecular drugs and macromolecular drugs. By tuning physical properties, such as degradability, charge density, crosslinking density, MAP gels can serve as not only a cell delivery vehicle and niche formation building blocks, but also as an *in situ* drug release platform for enhanced therapeutic effect (Fig. 6-1).

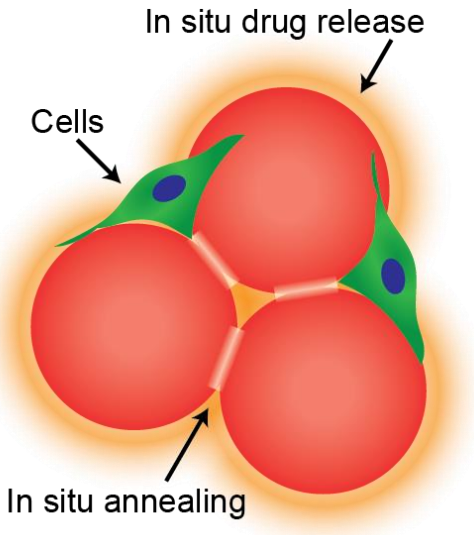

Figure 6-1 Drug release *in situ* from MAP scaffolds. MAP gels can serve not only as a physical tissue scaffolds, but also as a release therapeutic molecules to further enhance the efficacy of cell therapies.

6.2 Drug release methods

The main types of drugs for cell engineering include protein, peptide, DNA, RNA and chemicals, and they are different in their physical and chemical characteristics. These different characteristics can be utilized to release drugs in a sustainable and controllable way. The release methods have different mechanisms and release properties as shown in the figure 6-2. As a preliminary result, this study covers on the release of drug by diffusion and degradation mechanisms and suggests how the mechanisms can be implemented in MAP scaffolds.

The first mechanism for release is diffusion by controlling the hydrogel mesh size. Hydrogels consist of a crosslinked polymer network, and open spaces or meshes between polymer chains. Small molecules and solute can diffuse through the meshes, whose size spans from 5 to 100 nm[62]. The mesh size determines how drugs diffuse through a hydrogel, as it controls steric interactions between the drugs and the polymer network[21]. For the molecules that is smaller than the mesh, its release process is governed by diffusion and it is largely independent of the mesh size.

The second mechanism is release by degradation of hydrogels. If the drug size is approximately similar to the mesh size, the effect of steric hindrance becomes a dominant factor. By increasing the concentrations of the polymer crosslinking density, the mesh size can be further reduced such that drugs are encapsulated. Due to strong steric hindrance in this situation, drugs are less likely diffuse out from the gel mesh. The

diffusion only happens when the gel mesh size increases by degradation. Degradation can occur in the polymer backbone or at the crosslinks and is typically mediated by hydrolysis[63] or enzyme activity[64]. The degradation of hydrogel can be modulated by the type of backbones, type of crosslinkers, or crosslinking density.

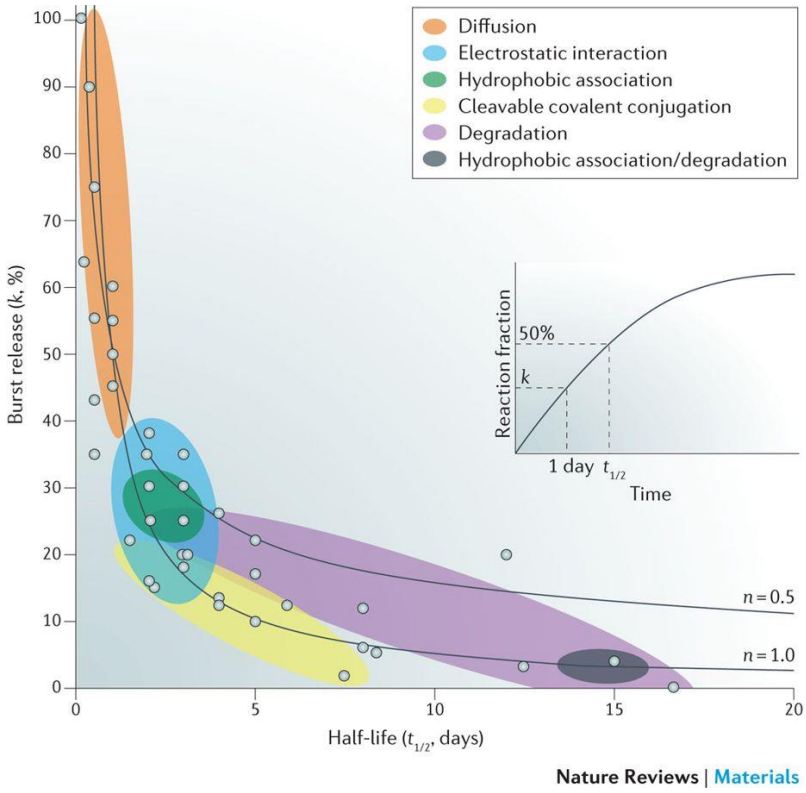

Figure 6-2 Drug release property chart of hydrogels. Each dot represents the burst release and half-life of release taken from the literature. The inset shows a representative release profile, for which the half-life ($t_{1/2}$) is determined by the time when the fraction of released drug reaches 50%, and the burst release parameter (k) is determined by the drug release fraction at 24 hours. The coloured circles refer to different drug release mechanisms: diffusion-controlled mechanism (orange), degradation-controlled mechanism (purple), affinity-controlled mechanisms based on cleavable covalent conjugation (yellow), electrostatic interactions (blue) and hydrophobic associations (green), as well as a combination of degradation-controlled and

hydrophobic association-controlled mechanisms (grey). Reproduced with permission from Springer Nature.

6.3 Macromolecule release from MAP scaffolds

As a model protein, the release of ovalbumin (OVA) from MAP gels was investigated. The ovalbumin protein of chickens consists of 385 amino acids, whose relative molecular mass is 42.7 kDa. Unheated OVA has average size about 6~7nm[65], which is comparable to the mesh size of MAP gels, resulting in a steric hindrance. Therefore, OVA proteins are most likely trapped by hydrogel mesh with more than 5wt% PEG concentration. The release of OVA from MAP gels was detected when 10% of TrypLE, a type of protease that degrades gel mesh, was present (Fig. 6-3). However, limited amount of OVA was released from MAP gels without TrypLE. This indicates that the macro molecules whose size is comparable with or larger than gel mesh are trapped in hydrogels and released in the response of gel degradation.

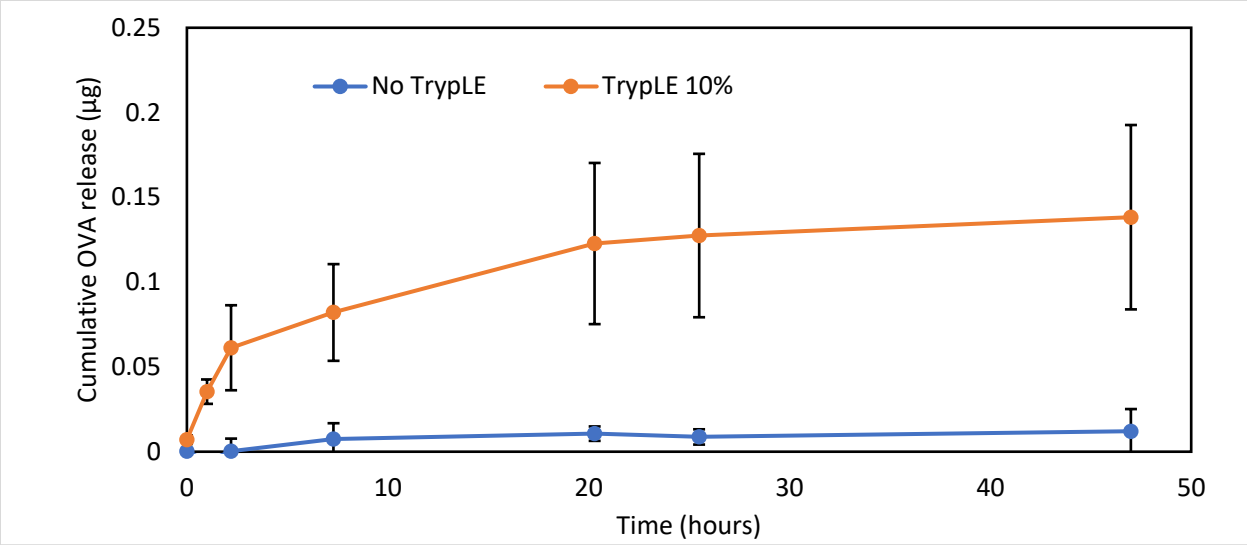

Figure 6-3 Release of ovalbumin (OVA) protein from MAP scaffold with and without protease, which degrades hydrogel mesh. OVA is released when MAP gels are degraded by protease added to buffer. (*n* = 3)

6.4 Small molecule release from MAP scaffolds

The release of enkephalin peptide was investigated to characterize the release of molecules smaller than the gel mesh. Enkephalin is a naturally occurring peptide that has potent painkilling effects and is released by neurons in the central nervous system and by cells in the adrenal medulla. Thus, delivering enkephalin peptide locally to a wound site with MAP scaffolds can not only accelerate the regeneration processes, but also reduce the pain while preventing the overuse of opioid. The molecular mass of enkephalin peptide is about 590 Da, which is expected to be much smaller than the gel mesh.

The half-life ($t_{1/2}$) of release of DADLE peptide, one of sub-types of enkephalin, was within a day in both of 5wt% and 10wt% PEG hydrogels. There was a delay in release with 10wt% PEG due to its smaller pore size. However, the release is faster than desired given the fact that the wound regeneration takes over the course of a week or so.

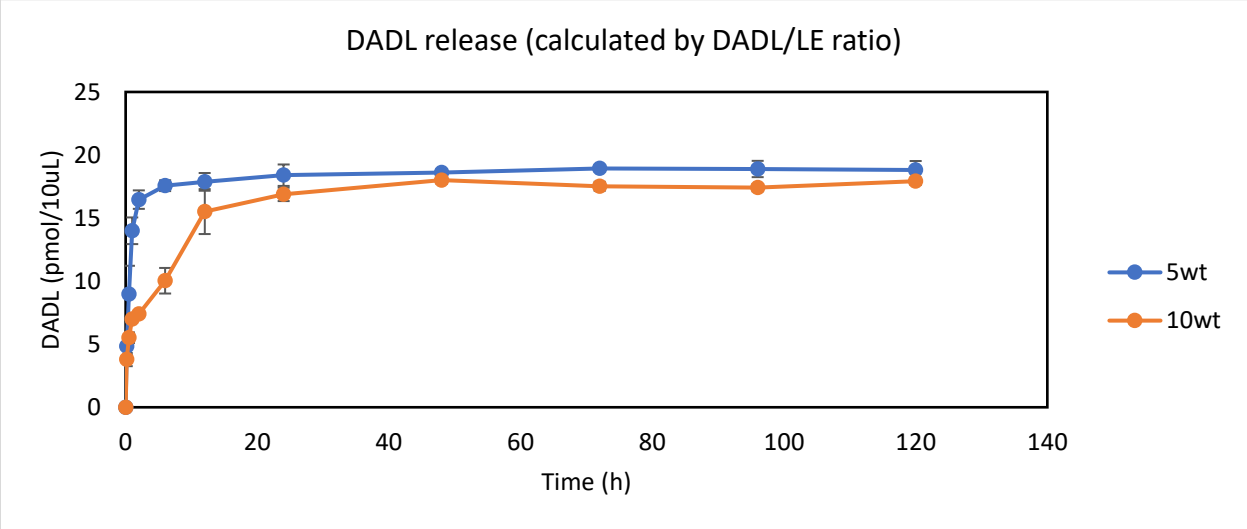

Figure 6-4 Release of DADL enkephalin peptide from MAP scaffolds with 5wt% or 10wt% PEG concentration. Due to small molecule size, the release of DADL is within a day without any degradation of gels. (n = 3)

6.5 PLGA encapsulation for small molecules

To control the release of small molecules smaller than gel mesh, poly lactic-co-glycolic acid (PLGA) nanoparticles can be used. PLGA is biocompatible and biodegradable, exhibits a wide range of erosion times, has tunable mechanical properties and is a FDA approved polymer[66,67]. Due to its tight mesh structure, it has been extensively studied

as delivery vehicles for drugs, various other small molecules such as DNA, RNA and peptides[68]. To encapsulate water-soluble drugs, water-in-oil-in-water emulsion methods are best suited such that PLGA capsule is formed to contain soluble drugs in the core (Fig. 6-5). The release of drugs encapsulated is mediated by PLGA copolymer degradation by hydrolysis or biodegradation through cleavage of its backbone ester linkages into oligomers and, finally monomers.

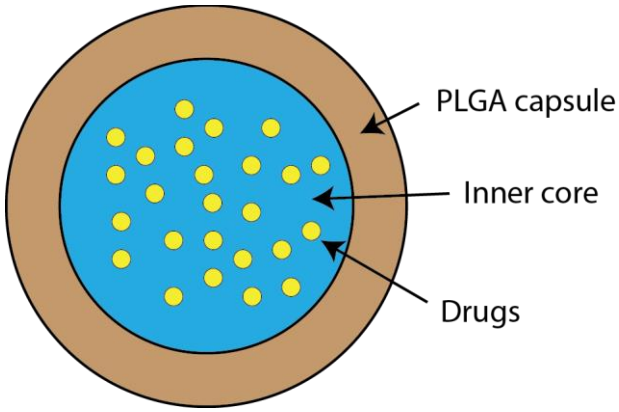

Figure 6-5 Water-in-oil-in-water emulsion method to encapsulate water-soluble drugs in PLGA particles. The release of drugs is mediated by the degradation of PLGA copolymer by hydrolysis or biodegradation.

PLGA particles can be encapsulated in MAP hydrogel mesh and perform as a drug carrier for sustained release. Typical size distribution of PLGA particles spans from a few nanometers to micrometers by controlling the stirring rates and conditions. To demonstrate the feasibility of encapsulating PLGA particles in MAP scaffolds, sub-micron size of PLGA particles with coumarin (green fluorescence) was mixed with 4-Arm PEG-VS solution. This solution is injected with crosslinker solution (dithiols) and pinched off by oil phase to generate droplets (Fig. 6-6a, b). Due to hydrophobicity and

higher density of PLGA than water, the dispersity of PLGA particles among MAP gels and within MAP gels was limited (Fig 6-6c), such that the amount of PLGA encapsulated in MAP gels was also limited. However, adding 0.1% of hyaluronic acid (HA) into pre-gel solution slowed down the settlement of PLGA particles in syringe so that it increased the dispersity of PLGA among MAP gels. Furthermore, transition of surface property of PLGA from hydrophobic to hydrophilic using PEG enhanced the dispersity of PLGA within MAP particles (Fig 6-6c).

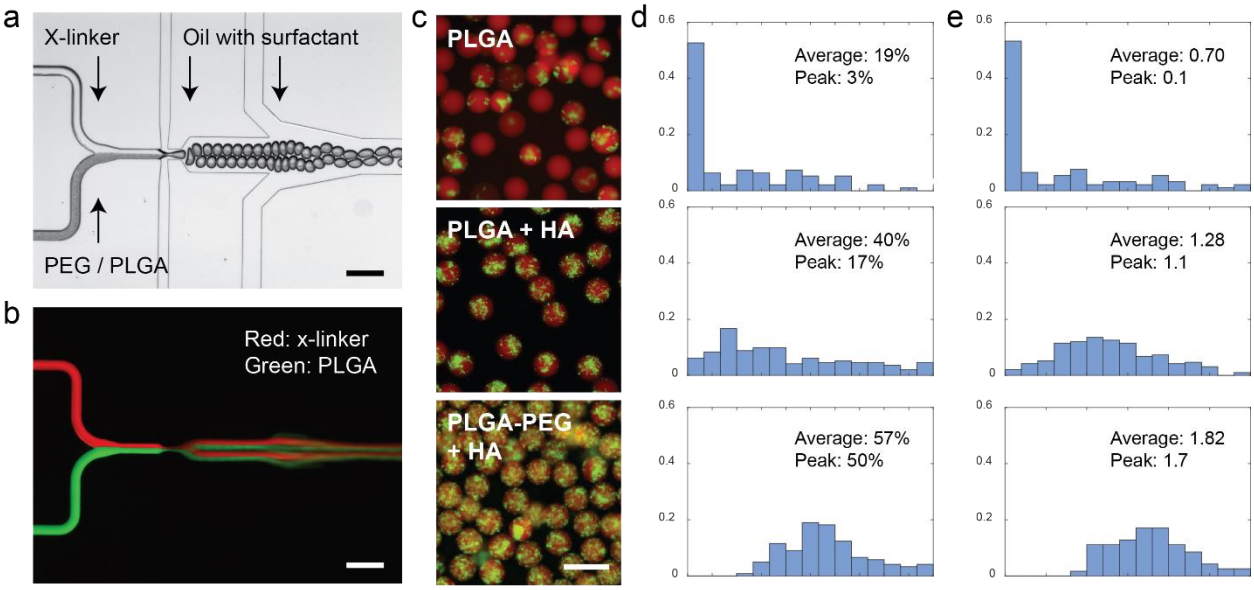

Figure 6-6 Microfluidic production of µgels with PLGA nanoparticles. **a**. Bright-field image of µgel production in the channel. Mixture of PEG and PLGA (top) and x-linkers (bottom)) are merged and pinched at the junction to generate monodisperse µgels. Scale bar: 200 µm. **b**, Fluorescent image of µgel production in the channel. Red: x-linker, green: PLGA. Scale bar: 200 µm. **c**, Fluorescent images of µgels with PLGA (top), PLGA + HA (middle), and PLGA-PEG + HA (bottom). Scale bar: 200 µm. **d**, Histogram of % area occupied by PLGA in µgels for dispersity within µgels. **e**, Histogram of total PLGA amount in µgels for dispersity among µgels.

Chapter 7. Concluding Remarks

The application of stem cell-based therapies has been limited by low retention rate of transplanted cells and lack of efficient control of the cell state and function. This study demonstrates increased *in vivo* maintenance of mesenchymal stem cells (MSCs) co-injected with a modular microporous scaffold made through the *in situ* crosslinking of flowable monodisperse hydrogel particles. Assemblies of spherical hydrogel building blocks created interconnected microscale void spaces which enhanced nutrient transport, and promoted cell migration and cell-cell connections, inducing more than ~7-times higher proliferation than chemically identical non-porous hydrogels *in vitro* and ~8-times enhanced MSC retention in a subcutaneous murine implantation model. Furthermore, independent modulation of the material properties of the building blocks, such as stiffness and adhesive ligand composition, resulted in conditions with higher production of therapeutically-active secretions accompanied by higher proliferation *in vitro* as well as increase in the maintenance of stem cells *in vivo*. Overall, we show that cell delivery in conjunction with an *in situ*-formed microporous niche promotes the survival of delivered cells and should enhance cell therapies in regenerative medicine and immunologic applications.

Appendices

Table 3 Details for statistical analyses. F indicates F-values for ANOVA tests, T indicates t-values for t-tests, and df indicates degrees of freedom.

Figure	Analysis	One-tailed or two-tailed	F or T, df
Fig. 2-3d 70kDa	One-way ANOVA	Two-tailed	F (2, 13) = 178
Fig. 2-3d 0.3kDa	One-way ANOVA	Two-tailed	F (2, 14) = 411
Fig. 2-3e	Student T-test	Two-tailed	T = 42.3217, df = 4
Fig. 4-1c	One-way ANOVA	Two-tailed	F (4, 15) = 153.19
Fig. 4-1d	One-way ANOVA	Two-tailed	F (4, 15) = 18.36
Fig. 4-1e	One-way ANOVA	Two-tailed	F (4, 15) = 33.5
Fig. 4-4b	One-way ANOVA	Two-tailed	F(2, 20) = 10.63 F(2, 20) = 20.88 F(2, 20) = 24.07 F(2, 16) = 5.18
Fig. 4-4c	One-way ANOVA	Two-tailed	F (2, 20) = 24.07
Fig. 4-4d	One-way ANOVA	Two-tailed	F (2, 20) = 9.79
Fig. 5-3b	One-way ANOVA	Two-tailed	F (3, 16) = 30.21
Fig. 5-3c	One-way ANOVA	Two-tailed	F (3, 12) = 7.16
Fig. 5-3f	One-way ANOVA	Two-tailed	F (3, 16) = 9.36

Fig. 5-3h	One-way ANOVA	Two-tailed	F (3, 16) = 16.38
Fig. 5-3i	One-way ANOVA	Two-tailed	F (3, 16) = 18.22
Fig. 5-8b	One-way ANOVA	Two-tailed	F (3, 15) = 4.720
Fig. 2	One-way ANOVA	Two-tailed	F (3, 12) = 37.5
Fig. 4-2b	One-way ANOVA	Two-tailed	F (4, 15) = 17.34
Fig. 5-1a	One-way ANOVA	Two-tailed	F (2, 6) = 384.28
Fig. 5-4a	One-way ANOVA	Two-tailed	F (3, 12) = 16.98
Fig. 5-4b	One-way ANOVA	Two-tailed	F (3, 12) = 15.2
Fig. 5-5c	One-way ANOVA	Two-tailed	F (3, 16) = 1.29
Fig. 5-5d	One-way ANOVA	Two-tailed	F (3, 16) = 0.59

Bibliography

1. Parekkadan, B. & Milwid, J. M. Mesenchymal Stem Cells as Therapeutics. *Annu. Rev. Biomed. Eng.* **12,** 87–117 (2010).

2. Trounson, A. & McDonald, C. Stem Cell Therapies in Clinical Trials: Progress and Challenges. *Cell Stem Cell* **17,** 11–22 (2015).

3. Tran, C. & Damaser, M. S. Stem cells as drug delivery methods: Application of stem cell secretome for regeneration. *Adv. Drug Deliv. Rev.* **82,** 1–11 (2015).

4. Ankrum, J. & Karp, J. M. Mesenchymal stem cell therapy: Two steps forward, one step back. *Trends Mol. Med.* **16,** 203–209 (2010).

5. Galipeau, J. & Sensébé, L. Mesenchymal Stromal Cells: Clinical Challenges and Therapeutic Opportunities. *Cell Stem Cell* **22,** 824–833 (2018).

6. Leach, J. K. & Whitehead, J. Materials-Directed Differentiation of Mesenchymal Stem Cells for Tissue Engineering and Regeneration. *ACS Biomater. Sci. Eng.* acsbiomaterials.6b00741 (2017). doi:10.1021/acsbiomaterials.6b00741

7. Barry, F. P. & Murphy, J. M. Mesenchymal stem cells: Clinical applications and biological characterization. *Int. J. Biochem. Cell Biol.* **36,** 568–584 (2004).

8. Baraniak, P. R. & McDevitt, T. C. Stem cell paracrine actions and tissue regeneration. *Regen. Med.* **5,** 121–143 (2010).

9. da Silva Meirelles, L., Fontes, A. M., Covas, D. T. & Caplan, A. I. Mechanisms involved in the therapeutic properties of mesenchymal stem cells. *Cytokine*

Growth Factor Rev. **20,** 419–427 (2009).

10. Teixeira, F. G., Carvalho, M. M., Sousa, N. & Salgado, A. J. Mesenchymal stem cells secretome: A new paradigm for central nervous system regeneration? *Cell. Mol. Life Sci.* **70,** 3871–3882 (2013).

11. Caplan, A. I. & Dennis, J. E. Mesenchymal stem cells as trophic mediators. *J. Cell. Biochem.* **98,** 1076–1084 (2006).

12. Madl, C. M., Heilshorn, S. C. & Blau, H. M. Bioengineering strategies to accelerate stem cell therapeutics. *Nature* **557,** 335–342 (2018).

13. Eggenhofer, E. *et al.* Mesenchymal stem cells are short-lived and do not migrate beyond the lungs after intravenous infusion. *Front. Immunol.* **3,** 1–8 (2012).

14. Burdick, J. A., Mauck, R. L. & Gerecht, S. To Serve and Protect: Hydrogels to Improve Stem Cell-Based Therapies. *Cell Stem Cell* **18,** 13–15 (2016).

15. Elman, J. S. *et al.* Pharmacokinetics of Natural and Engineered Secreted Factors Delivered by Mesenchymal Stromal Cells. *PLoS One* **9,** e89882 (2014).

16. Ranganath, S. H., Levy, O., Inamdar, M. S. & Karp, J. M. Harnessing the mesenchymal stem cell secretome for the treatment of cardiovascular disease. *Cell Stem Cell* **10,** 244–258 (2012).

17. Sun, Y., Chen, C. S. & Fu, J. Forcing Stem Cells to Behave: A Biophysical Perspective of the Cellular Microenvironment. *Annu. Rev. Biophys.* **41,** 519–542 (2012).

18. Vincent, L. G. & Engler, A. J. Stem cell differentiation: Post-degradation forces

kick in. *Nat. Mater.* **12,** 384–386 (2013).

19. Madl, C. M. & Heilshorn, S. C. Engineering Hydrogel Microenvironments to Recapitulate the Stem Cell Niche. *Annu. Rev. Biomed. Eng.* **20,** 21–47 (2018).

20. Mitrousis, N., Fokina, A. & Shoichet, M. S. Biomaterials for cell transplantation. *Nat. Rev. Mater.* **3,** 441–456 (2018).

21. Li, J. & Mooney, D. J. Designing hydrogels for controlled drug delivery. *Nat. Rev. Mater.* **1,** 16071 (2016).

22. Dimatteo, R., Darling, N. J. & Segura, T. In situ forming injectable hydrogels for drug delivery and wound repair. *Adv. Drug Deliv. Rev.* **127,** 167–184 (2018).

23. Shin, J. W. & Mooney, D. J. Improving Stem Cell Therapeutics with Mechanobiology. *Cell Stem Cell* **18,** 16–19 (2016).

24. Lutolf, M. P., Gilbert, P. M. & Blau, H. M. Designing materials to direct stem-cell fate. *Nature* **462,** 433–41 (2009).

25. Leach, J. B., Bivens, K. A., Patrick, C. W. & Schmidt, C. E. Photocrosslinked hyaluronic acid hydrogels: Natural, biodegradable tissue engineering scaffolds. *Biotechnol. Bioeng.* **82,** 578–589 (2003).

26. Drury, J. L. & Mooney, D. J. Hydrogels for tissue engineering: Scaffold design variables and applications. *Biomaterials* **24,** 4337–4351 (2003).

27. Tong, X. & Yang, F. Recent Progress in Developing Injectable Matrices for Enhancing Cell Delivery and Tissue Regeneration. *Adv. Healthc. Mater.* **7,** 1–16 (2018).

28. Kang, H.-W. *et al.* A 3D bioprinting system to produce human-scale tissue constructs with structural integrity. *Nat. Biotechnol.* **34,** 312–319 (2016).

29. Lough, D. *et al.* Regeneration of Vascularized Corticocancellous Bone and Diploic Space Using Muscle-Derived Stem Cells. *Plast. Reconstr. Surg.* **139,** 893–905 (2017).

30. Griffin, D. R., Weaver, W. M., Scumpia, P. O., Di Carlo, D. & Segura, T. Accelerated wound healing by injectable microporous gel scaffolds assembled from annealed building blocks. *Nat Mater* **14,** 737–744 (2015).

31. Koh, J., Wu, C.-Y., Kittur, H. & Di Carlo, D. Research highlights: microfluidically-fabricated materials. *Lab Chip* **15,** 3818–3821 (2015).

32. Okamoto, M. & John, B. Synthetic biopolymer nanocomposites for tissue engineering scaffolds. *Prog. Polym. Sci.* **38,** 1487–1503 (2013).

33. Bencherif, S. a *et al.* Injectable preformed scaffolds with shape-memory properties. *Proc. Natl. Acad. Sci. U. S. A.* **109,** 19590–5 (2012).

34. Griffin, D. R., Weaver, W. M., Scumpia, P. O., Di Carlo, D. & Segura, T. Accelerated wound healing by injectable microporous gel scaffolds assembled from annealed building blocks. *Nat Mater* **14,** 737–744 (2015).

35. Griffin, D. R., Weaver, W. M., Scumpia, P. O., Di Carlo, D. & Segura, T. Accelerated wound healing by injectable microporous gel scaffolds assembled from annealed building blocks. *Nat Mater* **14,** 737–744 (2015).

36. Sideris, E. *et al.* Particle Hydrogels Based on Hyaluronic Acid Building Blocks.

ACS Biomater. Sci. Eng. **2,** 2034–2041 (2016).

37. Nih, L. R., Sideris, E., Carmichael, S. T. & Segura, T. Injection of Microporous Annealing Particle (MAP) Hydrogels in the Stroke Cavity Reduces Gliosis and Inflammation and Promotes NPC Migration to the Lesion. *Adv. Mater.* **29,** 1–8 (2017).

38. Darling, N. J., Sideris, E., Hamada, N., Carmichael, S. T. & Segura, T. Injectable and Spatially Patterned Microporous Annealed Particle (MAP) Hydrogels for Tissue Repair Applications. *Adv. Sci.* **5,** 1–8 (2018).

39. Friedl, P. & Wolf, K. Plasticity of cell migration: A multiscale tuning model. *J. Cell Biol.* **188,** 11–19 (2010).

40. Kumar, N. N. *et al.* Relative vascular permeability and vascularity across different regions of the rat nasal mucosa: Implications for nasal physiology and drug delivery. *Sci. Rep.* **6,** 1–14 (2016).

41. Wong, A. P., Perez-Castillejos, R., Christopher Love, J. & Whitesides, G. M. Partitioning microfluidic channels with hydrogel to construct tunable 3-D cellular microenvironments. *Biomaterials* **29,** 1853–1861 (2008).

42. Wood, A. Preliminary host specificity testing of Endophyllum osteospermi (Uredinales, Pucciniaceae), a biological control agent against Chrysanthemoides monilifera ssp. monilifera. *Biocontrol Sci. Technol.* **16,** 495–507 (2006).

43. Sannino, A. *et al.* Synthesis and characterization of macroporous poly(ethylene glycol)-based hydrogels for tissue engineering application. *J. Biomed. Mater. Res.*

Part A **79A,** 229–236 (2006).

44. Soumpasis, D. M. Theoretical analysis of fluorescence photobleaching recovery experiments. *Biophys. J.* **41,** 95–97 (1983).

45. Aboufoul, M. & Garcia, A. Factors affecting hydraulic conductivity of asphalt mixture. *Mater. Struct. Constr.* **50,** 1–16 (2017).

46. Dong, H. & Blunt, M. J. Pore-network extraction from micro-computerized-tomography images. *Phys. Rev. E - Stat. Nonlinear, Soft Matter Phys.* **80,** 1–11 (2009).

47. Al-Kharusi, A. S. & Blunt, M. J. Network extraction from sandstone and carbonate pore space images. *J. Pet. Sci. Eng.* **56,** 219–231 (2007).

48. Chang, K. *Introduction to Geographic Information Systems*. (McGraw-Hill Science Engineering, 2006).

49. Hartsock, A. & Nelson, W. J. Adherens and tight junctions: Structure, function and connections to the actin cytoskeleton. *Biochim. Biophys. Acta - Biomembr.* **1778,** 660–669 (2008).

50. Williams, A. R. & Hare, J. M. Mesenchymal stem cells: Biology, pathophysiology, translational findings, and therapeutic implications for cardiac disease. *Circ. Res.* **109,** 923–940 (2011).

51. Fu, Y. *et al.* Trophic effects of mesenchymal stem cells in tissue regeneration. *Tissue Eng. Part B Rev.* **23,** ten.TEB.2016.0365 (2017).

52. Keung, A. J., Kumar, S. & Schaffer, D. V. Presentation Counts:

Microenvironmental Regulation of Stem Cells by Biophysical and Material Cues. *Annu. Rev. Cell Dev. Biol.* **26,** 533–556 (2010).

53. Gattazzo, F., Urciuolo, A. & Bonaldo, P. Extracellular matrix: A dynamic microenvironment for stem cell niche. *Biochim. Biophys. Acta - Gen. Subj.* **1840,** 2506–2519 (2014).

54. Hoch, A. I., Binder, B. Y., Genetos, D. C. & Leach, J. K. Differentiation-dependent secretion of proangiogenic factors by mesenchymal stem cells. *PLoS One* **7,** 1–10 (2012).

55. Ryan, A. E. *et al.* Chondrogenic differentiation increases antidonor immune response to allogeneic mesenchymal stem cell transplantation. *Mol. Ther.* **22,** 655–667 (2014).

56. Chen, X. *et al.* Chondrogenic Differentiation Alters the Immunosuppressive Property of Bone Marrow-Derived Mesenchymal Stem Cells, and the Effect Is Partially due to the Upregulated Expression of B7 Molecules. *Stem Cells* **25,** 364–370 (2007).

57. Guo, M. *et al.* Cell volume change through water efflux impacts cell stiffness and stem cell fate. *Proc. Natl. Acad. Sci.* **c,** 201705179 (2017).

58. Burdick, J. A. & Murphy, W. L. Moving from static to dynamic complexity in hydrogel design. *Nat. Commun.* **3,** 1–8 (2012).

59. Lee, J., Abdeen, A. A. & Kilian, K. A. Rewiring mesenchymal stem cell lineage specification by switching the biophysical microenvironment. *Sci. Rep.* **4,** 20–27

(2014).

60. Dong, H. K. *et al.* Gene expression profile of cytokine and growth factor during differentiation of bone marrow-derived mesenchymal stem cell. *Cytokine* **31,** 119–126 (2005).

61. Veiseh, O. *et al.* Size- and shape-dependent foreign body immune response to materials implanted in rodents and non-human primates. *Nat. Mater.* **14,** 643–651 (2015).

62. Lin, C. C. & Metters, A. T. Hydrogels in controlled release formulations: Network design and mathematical modeling. *Adv. Drug Deliv. Rev.* **58,** 1379–1408 (2006).

63. Boontheekul, T., Kong, H. J. & Mooney, D. J. Controlling alginate gel degradation utilizing partial oxidation and bimodal molecular weight distribution. *Biomaterials* **26,** 2455–2465 (2005).

64. Ishihara, M. *et al.* Controlled release of fibroblast growth factors and heparin from photocrosslinked chitosan hydrogels and subsequent effect on in vivo vascularization. *J. Biomed. Mater. Res. - Part A* **64,** 551–559 (2003).

65. Croguennec, T., Renault, A., Beaufils, S., Dubois, J. J. & Pezennec, S. Interfacial properties of heat-treated ovalbumin. *J. Colloid Interface Sci.* **315,** 627–636 (2007).

66. Makadia, H. K. & Siegel, S. J. Poly Lactic-co-Glycolic Acid (PLGA) as biodegradable controlled drug delivery carrier. *Polymers (Basel).* **3,** 1377–1397 (2011).

67. Bala, I., Hariharan, S. & Kumar, M. N. V. R. PLGA nanoparticles in drug delivery: the state of the art. *Crit. Rev. Ther. Drug Car. Syst.* **21,** 387–422 (2004).

68. Zhai. The manufacturing techniques of various drug loaded biodegradable poly(lactide-co-glycolide) (PLGA) devices. *Biomaterials* **21,** 2475–2490 (2000).